BABEȘ-BOLYAI UNIVERSITY

Faculty of Physics

Doctoral School of Physics

DOCTORAL THESIS

Summary

Impurity states in two-dimensional systems

Stanca-Georgeta MITRICI

Scientific leader

Prof. Dr. Leontin DAVID

Cluj-Napoca

2025

Thanks

The doctoral thesis was developed within the Doctoral School of Babeş-Bolyai University of Cluj-Napoca, Faculty of Physics, under the scientific supervision of Prof. Dr. Leontin David, to whom I extend my sincere thanks. for chance offered , for the trust given, the scientific guidance, the patience, the professionalism, the support, the coordination and the full understanding that he demonstrated throughout the entire process of preparing and writing the doctoral thesis.

I owe special gratitude to the members of the advisory committee: Prof. Dr. Mihai Todicã, Prof. Dr. Ioan Botiz, Prof. Dr. Grigore Damian, for the precious time given, for the valuable scientific advice, as well as for the competent and permanent guidance during the development and completion of this doctoral thesis.

I would also like to thank the team at the Department of Physics and Chemistry within the Faculty of Materials and Environmental Engineering for providing me with the necessary equipment to carry out the experimental part, namely spectrometers, diffractometer, adsorption device, and Assoc. Prof. Dr. Simona Rada for her availability for the support she provided and for contributing to my scientific training.

I would like to thank the distinguished professors who are members of the doctoral committee for accepting the proposal to be part of the public thesis defense committee and for the suggestions they made.

Thank you , family. my for love , understanding and the moral support provided throughout these years, providing me with the motivation and conditions necessary to complete and complete my doctoral thesis.

I thank everyone who, directly or indirectly, helped and supported me throughout the years in which I developed this work.

Mitrici Stanca-Georgeta

Table of contents

INTRODUCTION

1. Motivation for choosing the topic and carrying out the doctoral research

Glass has become a symbol of modern society, constantly evolving with special qualities such as high mechanical resistance to strong impact and stability at large temperature differences. Obtaining glass is a continuous process through which the development of the manufacturing field is closely correlated with the needs and daily concerns so that we enjoy the beauties of glass at every step, from tempered glass to optical fibers obtained from glass that allow the transmission of light signals at speeds of 111Gbyte/s.

2. Objectives of the doctoral thesis:

a. Impurification of lead-borate glasses (PbO_2) with nickel oxide (Ni_2O_3) in order to improve the optical and magnetic properties and obtain the physicochemical stability of the system;
b. Based glasses impregnated with iron oxide (Fe_2O_3) regarding the study of physicochemical properties, X-ray diffraction (XRD), Fourier Transform Infrared Spectroscopy (FTIR), ultraviolet-visible spectroscopy (UV-VIS), electron paramagnetic resonance spectroscopy (EPR), as well as acetylene adsorption on the surface of the samples;
c. Impurification of lead-borate glasses (PbO_2) with palladium in order to improve optical and mechanical properties, study carried out through experiment but also through molecular modeling with advanced chemistry-specific programs;
d. Impurification of lead-borate glasses (PbO_2) with palladium and alumina to improve heat resistance, anti-corrosion and electrical insulation properties by X-ray diffraction, FTIR spectroscopy, UV-VIS spectroscopy.

3. Organization and structure of the doctoral thesis

The doctoral thesis entitled **"Impurity States in Two-Dimensional Systems"** is structured in two main parts, the first part includes the theoretical notions of the specialty, and the second highlights the original contributions and is developed over seven chapters.

Chapter 1 entitled " **The current state of knowledge in the field of impure vitreous glasses** " presents general aspects regarding vitreous oxide materials, generalities, presents the method of undercooling melts and concepts regarding the structure of the vitreous state.

Chapter 2 entitled **"Methods for investigating the structural, optical, and magnetic properties of impure glass samples** ". This chapter presents the equipment used to determine the properties of the obtained systems and a classification of the physical analysis methods used in the doctoral thesis is made, namely X-ray diffraction, IR spectroscopy, RES spectroscopy, UV-VIS spectroscopy, determination of the optical gap energy and molecular modeling.

Chapter 3 entitled " **Glasses and glass-ceramics based on lead impregnated with nickel oxide** " synthesizes the structural, optical, spectroscopic and magnetic properties of glasses and glass- ceramics with the composition $xNi_2O_3 \cdot (100\text{-}x)[3B_2O_3 \cdot PbO_2]$ with x=5- 50 mol % Ni_2O_3.

X-ray diffraction investigation reveals the amorphous nature of samples with $x \leq 20$ % Ni_2O_3 and the presence of crystalline phases NiO and $Ni_3B_2O_6$ in samples with $x \geq 30$ mol% Ni_2O_3.

IR analysis demonstrates that increasing the Ni_2O_3 content of the samples results in the formation of BO-Ni bonds, orthoborate and $[NiO_6]$ structural units. By investigating with FTIR spectroscopy it was observed that acetylene can be adsorbed on the glass surface, reacting with water in the glass network resulting in acetaldehyde and acetic acid on the surface of the samples.

An important observation from the analysis of the UV-Vis spectrum of the nickel-lead-borate glass-ceramic system is that nickel ions absorb light in the region of 250 - 1000 nm. It was found that the value of the optical band energy (gap energy) varies between 4.21 and 4.34 eV . increasing the Ni_2O_3 content in the composition range $10 \leq x \leq 30$ mol% Ni_2O_3 occurs an enhancement of the resonance line at g~2.21, due to Ni^{+2} ions . This EPR resonance line was not observed for samples with x=5 and 50 mol% Ni_2O_3.

The glass-ceramic sample x=30% Ni_2O_3 effective magnetic moment per nickel ion becomes larger than that of the samples with x<30% mol Ni_2O_3 suggesting a superparamagnetic behavior. This hypothesis is supported by the magnetization versus magnetic field variation and is due to the formation of crystalline phases of NiO and $Ni_3B_2O_6$.

Chapter 4 entitled " **Iron Oxide-Doped Lead-Based Glasses and Glass-Ceramics** " presents a new system for applications in solar cells and the adsorption of small molecules, such as acetylene, on iron-lead-borate glasses and glass-ceramic surfaces. In this regard, glasses and glass-ceramics for the system $xFe_2O_3 \cdot (100\text{-}x)[3B_2O_3 \cdot PbO_2]$ with x=5-50mol% Fe_2O_3 were synthesized by the melt quenching method and characterized to obtain information about the

structural correlations and the relationship between the structure and the physical properties of these materials. The effect of adding iron ions in the host matrix together with the effect of the matrix on the paramagnetic behavior were investigated using X-ray diffraction (XRD), Fourier transform infrared spectroscopy (FTIR), ultraviolet-visible spectroscopy (UV-Vis) and electron paramagnetic resonance (EPR) spectroscopy. The XRD pattern for the prepared samples shows their glassy nature only for x≤30mol% Fe_2O_3. For samples containing 40 mol% Fe_2O_3, the presence of the crystalline phase a-Fe_2O_3 embedded in the - an amorphous matrix. IR data suggest that the addition of high iron(III) oxide content to the host matrix leads to gradual conversion into $[PbO_4]$, $[PbO_3]$, $[BO_4]$, $[BO_3]$ structural units and the formation of $[FeO_n]$ structural units through changes in the Pb-OB and Pb-O-Pb bending vibrations.

UV-Vis data show that adding a higher concentration of Fe_2O_3 produces a gradual shift in absorption to the longer wavelength side, indicating absorption light from 295 to 1050 nm and a decrease in the bandgap energy.

The EPR spectra show resonance signals at g~4.3 and g~2 indicating the presence of ions Fe^{+3} in sites with distorted octahedral symmetry and as well as in clustered formations containing both Fe^{+3} and Fe^{+2} ionic species.

Chapter 4 entitled " **Palladium - doped lead- based glasses and glass- ceramics** " summarizes the structural, optical, spectroscopic and adsorption properties of glasses and glass-ceramics with the composition xPd•(100-x) $[3B_2O_3 \bullet PbO_2]$ that were synthesized in the composition range $5 \leq x \leq 40$% mol Pd. The chapter also includes density functional calculations on ethylene adsorption on small clusters of Pd_n, n=1-6 applied for two types of π and di-σ adsorption depending on the cluster size, $C_2H_2Pd_n$, by molecular modeling using the Gaussian program.

Chapter 6 entitled " **Glasses and glass-ceramics based on lead impure with aluminum oxide and palladium** " synthesizes the structural, optical, spectroscopic properties of glasses and glass-ceramics with the composition xPd_Al_2O_3•(100-x) $[3B_2O_3 \bullet PbO_2]$ that were synthesized in the composition range $5 \leq x \leq 50$% mol Al_2O_3. By adding small amounts of aluminum oxide (Al_2O_3) and boron trioxide (BO_3), glasses resistant to sudden temperature variations are obtained and are used in the manufacture of laboratory vessels. The alumina introduced into the glass provides high thermal stability and a high specific surface. These glasses have a very high chemical resistance and a low expansion coefficient. Among the most famous glasses obtained by

doping with aluminum oxide, we mention: Jena, Pyrex or Duran. Aluminum oxide is well known as a glass-ceramic material for its excellent properties such as high heat resistance, excellent anti-corrosion properties and good electrical insulation. Aluminum oxide glass-ceramics are used in the manufacture of wear-resistant parts as well as electrical insulators and furnace linings. For example, its dielectric property in electronics makes this material suitable as an insulator in integrated circuits.

The general conclusions, personal contributions and proposals for future research directions are contained in Chapter 7 entitled ***"General Conclusions"*** , systematically presenting the most important conclusions and personal contributions drawn from the research undertaken.

The exploitation of the obtained results was materialized by the elaboration of a number of *2 articles* , published in ISI journals: "Acetylene adsorption on the iron-lead-borate glassy and vitroceramic surface", " Nickel-lead-borate glasses and vitroceramics with antiferromagnetic NiO and nickel-orthoborate crystalline phases " and *the oral presentation entitled "* Adsprbtion of acetylene on lead-based glass and glass-ceramic surfance doped with nickel and palladium *"* during an international conference held in Timişoara, TIM 24 Physics Conference, June 1, 2024

The experimental part took place in the laboratories of the Department of Physics & Chemistry within the Faculty of Materials and Environmental Engineering at the Technical University of Cluj-Napoca, located on Muncii Boulevard no. 103-105.

PART I: THEORETICAL NOTIONS OF SPECIALTY

CHAPTER 1. CURRENT STATE OF KNOWLEDGE IN THE FIELD OF IMPURIFIED GLASS SYSTEMS

1.1. Vitreous oxide materials

1.1.1. Structure of B_2O_3 glass

Glass is defined as an "inorganic fusion product that has been cooled under rigid conditions without crystallizing . " Glass or vitreous materials can also be defined as "amorphous solids without periodicity in the arrangement of atoms" or "noncrystalline solids obtained by freezing a cooled liquid ." The term noncrystalline solid suggests the idea that glasses cannot be classified either in the category of crystalline materials such as quartz or sapphire or in the category of liquids. In general, they are defined as solids that have a locally uniform geometric arrangement at short distances , but the periodic arrangement is absent at long distances . In other words, the atomic arrangement in glasses is intermediate between that of crystalline materials and liquids.

1.1.2. Melt subcooling method

The most commonly used method for preparing oxide glasses is to undercool the melts, i.e. to cool them below the solidification temperature without causing nucleation and consequently crystallization. This results in a kind of "freezing" of the melt, so that, in general, the disordered structure existing in the melts (in the liquid state) is preserved in the solid state of the glass.[3]

This method consists of melting the mixture of raw materials obtained according to the oxide chemical composition, maintaining the melt for a determined period of time at a well-established equilibrium temperature and cooling it rapidly. In research laboratories, cooling of the samples is achieved by pouring the melts onto a copper or stainless steel plate (or molds of the desired shape), which is at room temperature (or lower temperatures) and sometimes by applying another plate of the same nature.

CHAPTER 2. METHODS FOR INVESTIGATING ROPTHE OPTICAL AND MAGNETIC STRUCTURAL PROPERTIES OF IMPURIFIED GLASS SAMPLES

2.1. X-ray diffraction

X-ray diffraction is one of the most reliable methods to determine whether a material is crystalline or amorphous, which allows obtaining information about the local and intermediate order of the structure. The information obtained from X-ray scattering differs depending on its type. Elastic scattering provides, by studying the angular dependence of the scattered radiation intensity, information about the spatial distribution of the scattering centers, while inelastic scattering provides information about the dynamics of the system.[12]

The position of this very broad maximum is not necessarily the position of the most intense maximum in the diffractogram of the same sample in the crystalline state.

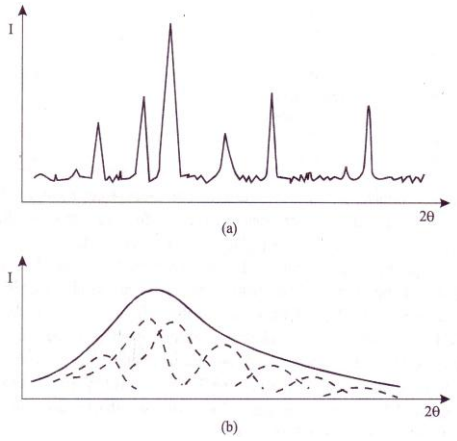

Fig. 2.1. Modification of the diffraction image following amorphization:

a. diffractogram of a polycrystalline material; b. diffractogram of the same material in the amorphous state – the dotted curves represent the initial maxima, from the crystalline sample, broadened following amorphization to the point of overlap

2.2. Infrared Spectroscopy (IR)

IR spectroscopy has found wider application in recent decades in the analysis of the structural properties of impure glasses. It is not only applied to crystalline substances, but is also used in the investigation of non-crystalline phases. IR absorption spectra are used for research into the structure of glasses for both qualitative and quantitative analyses.

The basic principle of IR spectroscopy consists of irradiating the sample and measuring the absorption of the rays as they pass through it.

Infrared radiation is invisible radiation, characterized mainly by its caloric properties, having been discovered in 1800 by FH Herschel. They have wave numbers between approx. $1.3 \cdot 10^{4}$ cm^{-1} and $0.3 \cdot 10^{2}$ cm^{-1}. The energies of infrared radiation have values between approx. 0.003 eV and 1.6 eV.

2.3. Ultraviolet and Visible Spectroscopy (UV-VIS)

Ultraviolet-visible spectroscopy involves the absorption of light radiation in this range by molecules of organic and inorganic substances, absorption which results in the promotion of electrons in the σ, π or n orbitals from a low energy state to an excited state (richer in terms of energy). Due to the energies involved, transitions also occur between vibrational and rotational levels, so that the spectra in question are actually electronic vibrational and rotational spectra characterized by broad bands. The ultraviolet range includes radiation with wavelengths ranging from 100-380 nm, and the visible range includes radiation with wavelengths ranging from 380-780 nm. Another significant range is that between 200 - 300 nm, called quartz ultraviolet (ultraviolet), for which the vast majority of UV spectrometers are built, and the 380 - 800 nm range, in which substances that appear colored to the human eye absorb.

2.4. Determination of the optical gap energy

In ***amorphous materials,*** the absorption due to band-to-band transitions that determine the optical gap energy was interpreted by ***Davis and Mott*** . The expression for the absorption coefficient, α, as a function of the light wave energy, hν, is as follows:

$$\alpha = \alpha_0 / h\nu \, (h\nu - E_g)^n = B(h\nu - E_g)^n \qquad (2.10)$$

where α is the absorption coefficient, $\alpha_0/h\nu=B$ is a constant, E_g is the optical gap energy. Quite frequently this relationship gives a fairly satisfactory description of absorption in this range of wavelength values.

The absorption coefficient, α, can be determined from the relationship α=2.303A/d, where A is the absorbance and d is the sample thickness. [21-23]

The band gap energy E_g is obtained by plotting $(\alpha h\nu)^n$ as a function of the photon energy (hν) (where n takes different values depending on the optical transitions that occur, as follows: n=2 for the direct allowed transition, n=1/2 for the indirect allowed transition, n=1/3 for the indirect forbidden transition and n=2/3 the direct forbidden transition) and extrapolating the linear portion of the curve for $(\alpha h\nu)^n = 0$.

Experimental E_g if expressed in eV can be calculated from the formula:

$$E_g = 1240/\lambda \quad (2.11)$$

2.5. Electron Spin Resonance Spectroscopy (ESR)

Electron spin resonance (ESR) or electron paramagnetic resonance (EPR) is the study of molecules containing unpaired electrons by observing the magnetic fields at which they resonate with monochromatic radiation. These names are equivalent and simply emphasize different aspects of the same phenomenon that requires the presence of a kinetic moment in the sample under study. This kinetic moment can be spin and is due to the unpaired electrons of the atoms and molecules of the studied systems or to an orbital corresponding to the p, d or f orbitals of atoms in the gaseous state or being part of different molecules [23]. Therefore, ESR spectroscopy is a physical method of analysis that is based on the absorption of energy from the microwave range by a system of paramagnetic ions (containing unpaired electrons) placed in a magnetic field. The property of some bodies to magnetize when introduced into a magnetic field is called paramagnetism [24].

2.6. Molecular modeling

To evaluate the integrative potential of physicochemical transformations, experimental investigation techniques such as X-ray diffraction, FT-IR, UV-VIS, NMR and RES spectroscopies are used, as well as molecular modeling techniques. Theoretical, molecular modeling techniques

for evaluating the integrative potential of physicochemical transformations are based on Ab Initio calculations, density functional theory (DFT methods) and semi-empirical methods. From such combined studies, the geometric structure of molecules or molecular clusters is obtained, as well as their properties such as: dipole, quadrupole moments, etc., rotational constants, partial atomic charges, energies and shapes of molecular orbitals, ionization energies and of course vibrational spectra, UV-VIS, IR, RES, NMR. Different conformers of molecules can be analyzed, intermolecular interactions, solution-solvent interactions or molecule-adsorbent layer interactions can be studied. The study of intra- and intermolecular hydrogen bonds is also one of the main objectives of such studies.

From a theoretical point of view, we pursue studies in which we determine the optimal exchange and correlation functionals to be used in the calculation of various molecular properties by DFT methods. We are also interested in determining basis sets that perform as well as possible both in terms of the accuracy with which molecular properties are calculated and in terms of the required computational resources. Finally, we are interested in the development of hybrid methods for calculating molecular structure and properties, combinations of semiempirical (fast) and non-empirical (highly accurate) methods that offer a good compromise in theoretical studies of molecules with a large number of atoms. [27]

PART II: ORIGINAL CONTRIBUTIONS

CHAPTER 3. LEAD-BASED GLASS AND GLASS-CERAMICS IMPURIFIED WITH NICKEL OXIDE

3.1.Introduction

Lead oxide glasses have the ability to form stable glasses due to the dual role played by lead ions. Thus, lead ions can play both the role of modifier of the glass network when the Pb-O bonds present a predominant ionic character, and, respectively, the role of glass former when providing structural units [PbO_4] and Pb-O bonds with a predominantly covalent character [36].

It is generally accepted that only Ni^{+2} ions with the $3d^8$ electronic configuration are stable in glasses under normal atmospheric conditions [37]. Thus, nickel usually occurs in glasses as Ni^{+2} ions which can exist in tetrahedral and octahedral coordination sites, depending on the composition of the host glasses [38]. In general, in glasses, Ni^{+2} ions strongly favor octahedral coordination over tetrahedral coordination because the former has a particularly high crystal field stabilization energy. On the other hand, the different colors of glasses containing nickel are mainly caused by the appearance of two color centers, namely the structural units [NiO_6] and [NiO_4], and a change in the equilibrium between these centers can be recognized. The equilibrium between the two color centers depends on the composition of the glass [39].

3.2. Experimental procedure

For the preparation of lead borate glasses doped with nickel oxide and associated glass-ceramics , H_3BO_3, PbO2 and Ni_2O_3 of high purity [33]. The samples were synthesized by melting appropriate amounts of raw materials at $1150\ ^0C$ using an electric furnace, in a sintered corundum crucible. After 10 minutes, the molten material was quenched at room temperature by pouring onto a stainless steel plate.

The obtained materials were characterized by X-ray diffraction using a Shimadzu XRD-6000 diffractometer, with a graphite monochromator for Cu-Kα radiation (λ=1.54Å), at room temperature.

FT-IR spectra of the glasses were obtained in the spectral range of 350-2000 cm^{-1} with a JASCO FTIR 6200 spectrometer using the standard KBr bead disk technique. The spectra were obtained with a standard resolution of 2 cm^{-1}.

UV-Visible absorption spectra of powdered glass samples were recorded at room temperature in the range of 250-1050 nm using a Perkin-Elmer Lambda 45 UV/VIS spectrometer equipped with an integrating sphere. These measurements were made on glass powder dispersed in KBr pellets. The band position validity is ±2nm.

EPR measurements of powder samples were performed with a Bruker ELEXSYS 500 X-band spectrometer (9.52 GHz). Spectra were measured in the temperature range 110-300 K using a variable temperature accessory. EPR spectra processing was performed by software. EPR spectra were recorded using equal amounts of samples.

Magnetic susceptibility measurements were performed using a Faraday balance in the temperature range 80 - 300 K. The measurements were performed on samples with a mass of $11.7 \cdot 10^{-3}$ to $19.4 \cdot 10^{-3}$ g.[41]

3.3. Results and discussions

3.3.1. Investigation by X-ray diffraction

The X-ray diffraction patterns of the samples $xNi_2O_3 \cdot (100-x)[3B_2O_3 \cdot PbO_2]$ with x=5-50 mol% Ni_2O_3 are shown in Fig. 3.1. Figure 3. 1.a) does not display distinct diffraction peaks confirming the amorphous nature of the samples with doping between $5 \leq x \leq 20$mol% Ni_2O_3. For the sample x=30mol% Ni_2O_3, the XRD diffractogram shows the presence of crystalline phases $Ni_3B_2O_6$ and NiO with weak crystallinities (Fig. 3.1.b). When the Ni_2O_3 content is increased to 50 mol%, the crystalline phase $Ni_3B_2O_6$ with good crystallinity was found to coexist with the crystalline phase NiO with rhombohedral lattice.[42]

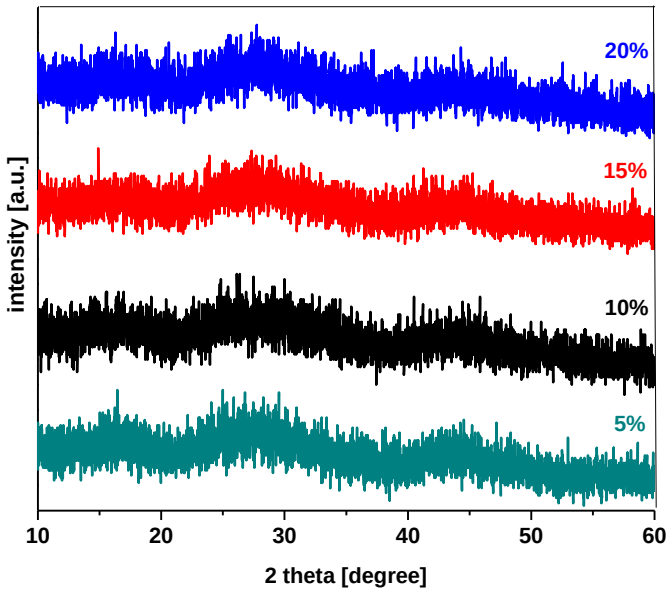

Fig. 3.1.a): XRD diffractograms of the system $xNi_2O_3 \cdot (100 - x)[3B_2O_3 \cdot PbO_2]$ in which x = 5-50mol% Ni_2O_3

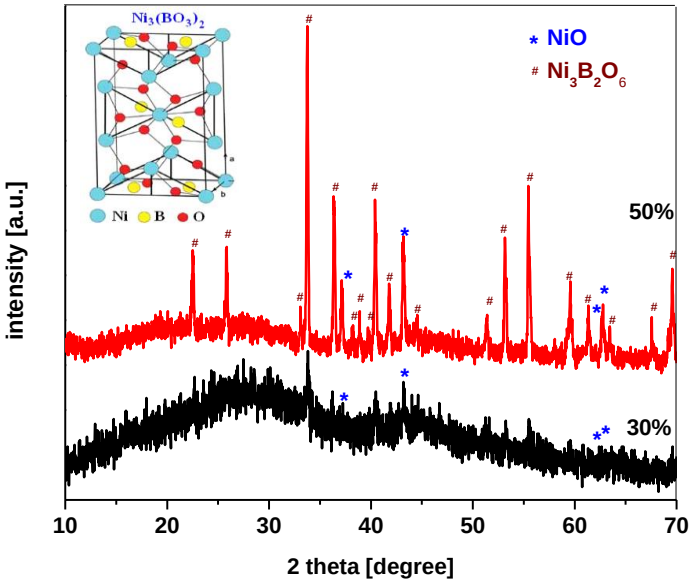

Fig.3.1.b) The XRD diffractogram shows the presence of the crystalline phases $Ni_3B_2O_6$ and NiO

3.3.2. FTIR spectroscopy

Figure 3.2. reveals the FTIR infrared absorption spectra of the glass-ceramic system $xNi_2O_3(100-x)[3B_2O_3 \cdot PbO_2]$ in where x=0-50 mol % Ni_2O_3.

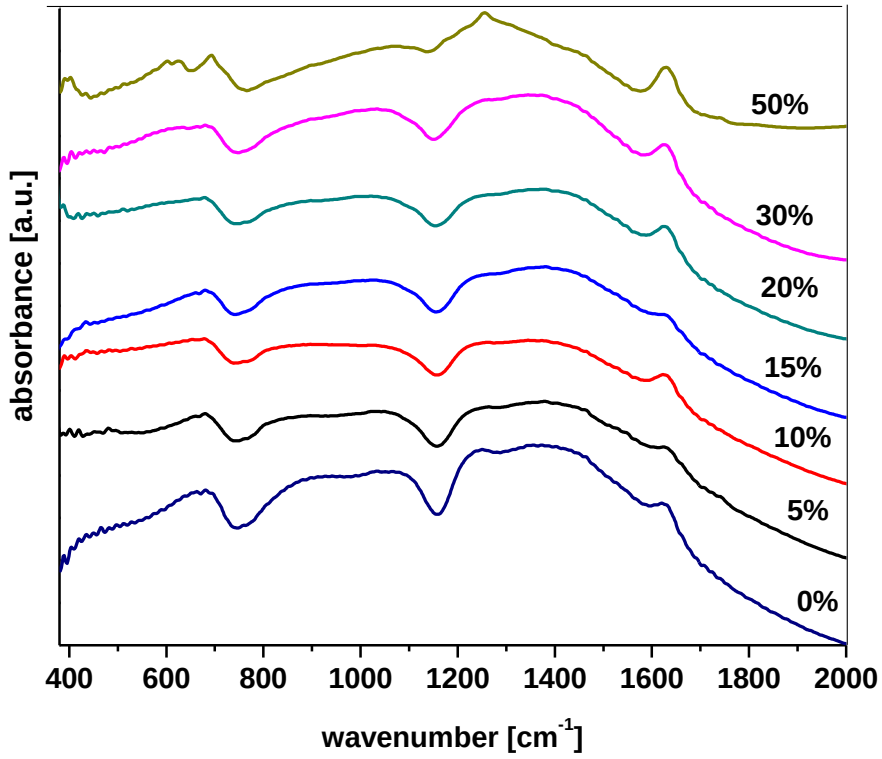

Fig.3. 2 FTIR spectra of $xNi_2O_3 \cdot (100-x)[3B_2O_3 \cdot PbO_2]$ glass / glass ceramics where x =5-50 mol % Ni_2O_3

The presence of new IR bands located at ~600, ~630, ~695 and ~1254cm $^{-1}$ in the x=50mol% sample suggests the presence of the $Ni_3B_2O_6$ crystalline phase, in agreement with the XRD data. The IR bands located at lower wavenumbers correspond to the in-plane and out-of-plane BO bending vibrations, and the last band is assigned to the asymmetric B-O stretching vibrations present in the triangular [BO_3] orthoborate units [62].

As the Ni_2O_3 concentration increases to 50 mol%, it is observed that the intensity of the IR bands due to the [BO_4] stretching vibrations increases, while progressive changes in the intensity of the boroxol rings and the [BO_3] structural units can be observed. These structural

changes indicate the gradual transformation of the nickel ion environment from the tetrahedral to the octahedral environment and the formation of orthoborate structural units, in agreement with the XRD data. [63-65]

In short, the addition of a higher content of Ni_2O_3 results in the reduction of the amount of BOB bonds due to the gradual transformation into orthoborate structural units, which decreases the connectivity of the lead-borate network. The accommodation of the host network with oxygen atoms can be achieved by the formation of [NiO_6] structural units.

3.3.3 UV-VIS spectroscopy

Pb +2 ions with the $6s^2$ electronic configuration absorb strongly in the ultraviolet region with an absorption band centered at 310 nm, due to the allowed parity of the $6s^2$ - 6sp transition.[66]

Divalent nickel in octahedral coordination gives a spin-allowed absorption band located at ~425nm corresponding to the $3a_{2g}(F) \rightarrow 3t_{1g}(P)$ transition and a very weak spin-forbidden transition $3a_{2g}(F) \rightarrow 1e_g(D)$ centered at ~780nm, accompanied by a very weak yellow glass color. Tetrahedrally coordinated Ni + 2 ions exhibit intense UV - Vis absorption bands at approximately 620nm and 1040nm [67-68].

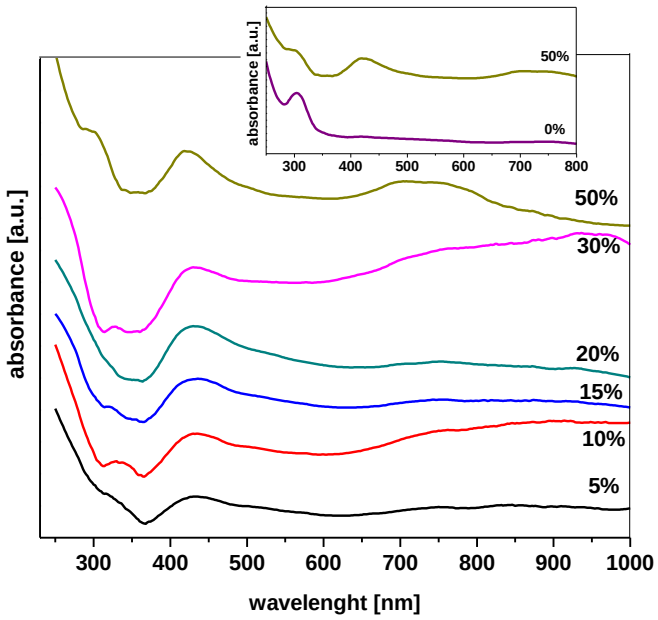

Fig.3.3. UV-VIS spectra of xNi203 · (100 -x)[3B203 · PbO2] glasses / glass-ceramics where x= 5-50 mol % Ni203.

The UV-Vis of the studied lead borate host glass exhibits a strong absorption band in the UV region without visible and infrared maxima, as shown in Fig. 3.3. By increasing the nickel oxide content of the samples up to 30 mol%, absorptions centered at ~430, ~750 and ~950 nm were observed in the UV-Vis. The increase in the intensity of the UV-Vis band located between 450 and 500 nm suggests the increase in the concentration of bonding oxygen ions. This is also accompanied by an increase in the band gap, consistent with the energy data of the optical gap.

3.3.4. Optical gap energy

Figure 3.4. shows the indirect dependence of the band gap energy on the nickel oxide content of the prepared glasses and glass-ceramics. It is found that the band gap energy value varies between 4.21 and 4.34 eV. An increase in the optical gap energy is observed in the samples with x=10 and 30% mol Ni_2O_3. The indirect band gap energy becomes higher due to the decrease in the concentration of unbound oxygen ions.

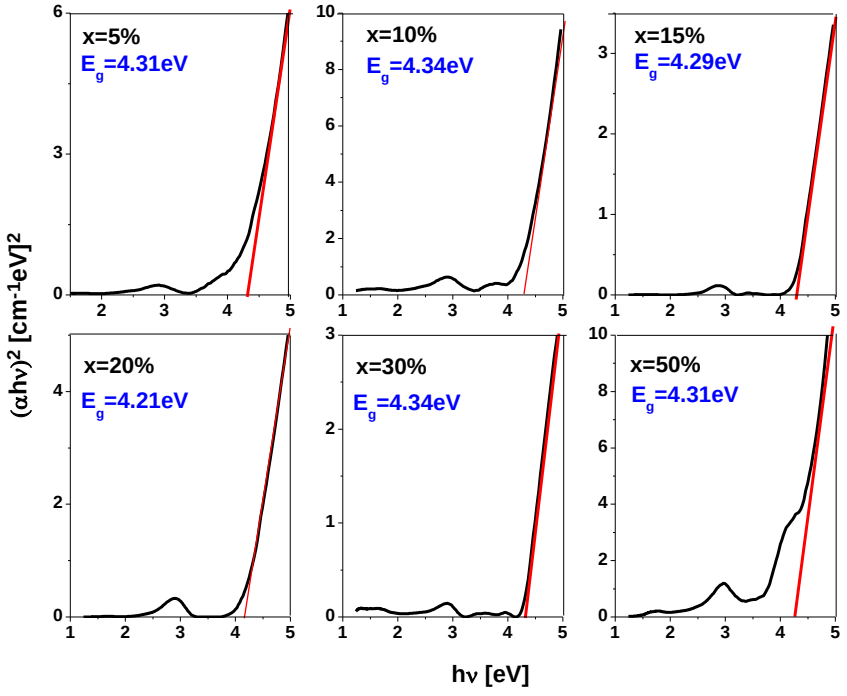

Fig.3.4. Graphs of $(\alpha h\nu)^2$ versus *hν* for the xNi_2O_3 system $\cdot (100 - x)[3B_2O_3 \cdot PbO_2$ where x = 5-50mol% Ni_2O_3. Linear extrapolation of the optical range energy, E_g

3.3.5. EPR spectroscopy

Figure 3.5.a shows the EPR spectra of samples from the system $xNi_2O_3(100-x)[3B_2O_3 \cdot PbO_2]$ where x varies between 10% and 50% Ni_2O_3. These spectra were recorded in the X-band, at room temperature.

EPR spectra , $xNi_2O_3 \cdot (100-x)[3B_2O_3 \cdot PbO_2]$ It exhibits two broad absorptions located at g≈2.21 and g≈8, respectively . [73]

The first EPR absorption, namely the one located at g≈2.21, appears only in the spectra of samples with x=15% and x=30% Ni_2O_3. The intensity and linewidth of this EPR resonance line are influenced by the Ni_2O_3 content of the samples. No EPR line centered at *g≈2.21* was observed for x=5%, 10% and 50 % Ni_2O_3.

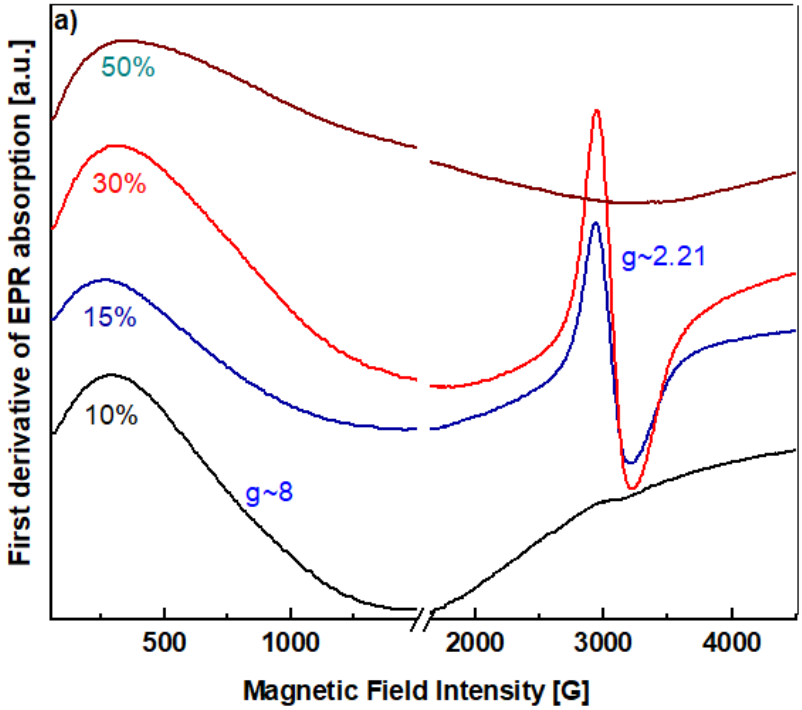

Fig.3.5.a) EPR spectra of the system $xNi_2O_3 \cdot (100-x)[3B_2O_3 \cdot PbO_2]$ where x = 10 , 20 and 50 mol% Ni_2O_3

EPR studies on oxide glasses containing nickel ions have shown that these ions always appear in their 2+ valence state, regardless of the nickel compound used as the starting material.

As mentioned, the EPR spectra of Ni 2+ ions in oxide glasses consist of a single asymmetric resonance line normally located at g ≈ 2.10–2.38. This has been observed for Ni $^{2+}$ ions in silica glasses, soda-boric glasses, lithium fluoroborate glasses, zinc phosphate glasses, sodium phosphate glasses, lead-borate glasses, and nickel-strontium-borate glasses [74–80]. In the case of lithium bismuth borate glasses [76] an EPR absorption located at g ≈ 2.70 has been recorded. The large deviation from normal g values that occurs for lithium bismuth borate glasses is due to spin-orbit coupling and the influence of the microneighborhood of Ni 2+ ions and b. the superexchange interactions between Ni ions (via nonmagnetic O $^{2-}$ ions) which decrease the resonant field and increase the value of the g factor.

The above-mentioned behavior of nickel ions suggests that their most stable valence state in oxide glasses is 2+. Thus, regardless of their initial valence state imposed by the raw material used for sample preparation, an intense reduction/oxidation process will transform these ions into their 2+ valence state.

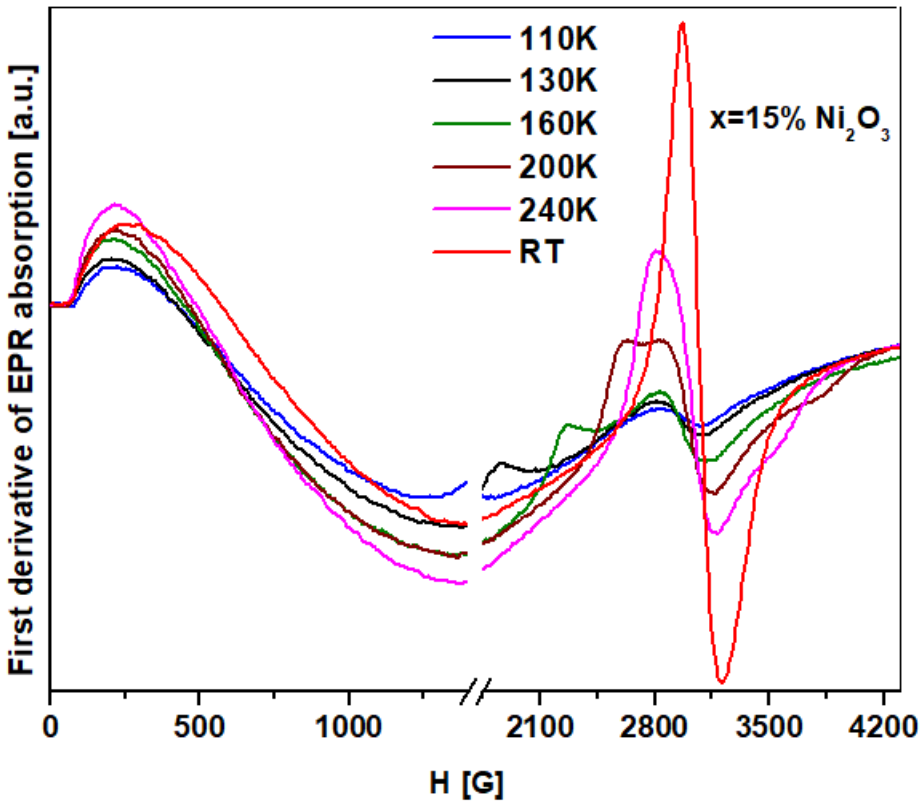

Fig.3.5.b) Temperature dependence of EPR spectra for sample x=15mol% Ni $_2$ O $_3$.

All of these ion species are paramagnetic and can provide EPR spectra at room temperature. These spectra typically consist of a single broad absorption line with relatively similar g values, ranging from 2.10 to 2.38 [73]. Because of this, assigning the EPR signal to a specific nickel ion valence state based on the g value alone is very difficult, if not impossible.

Figure 5a shows that by increasing the nickel(III) oxide content of the samples from x=15% to x=30%, the linewidth of the EPR resonance line at g ≈2.21 decreases slightly. As is known, the linewidth of the EPR signal is influenced by several mechanisms leading to line broadening (dipole-dipole interactions, increased structural disorder) or line narrowing (exchange/superexchange interactions). Depending on the doping level of the EPR active ions, some of these mechanisms may become predominant. In our case, the narrowing of the EPR signal with increasing Ni_2O_3 content of the samples is due to the increase in the intensity of superexchange interactions between paramagnetic nickel species (mainly Ni^{2+}, but also Ni^{3+} and Ni^{+}).[75]

Figure 3.5.b shows the EPR spectra recorded for the sample x = 15 mol% Ni_2O_3 at different temperatures between 110 K and room temperature (RT). The temperature evolution of these spectra reveals a dramatic decrease in the intensity of the resonance line from g≈2.21 accompanied by a shift to lower magnetic fields. This evolution confirms our hypothesis that most of the nickel ions present in the studied samples are in the 2+ valence state and that the other nickel species (clusters/nanoparticles of Ni^{3+}, Ni^{+} and Ni^{0}) are present in small amounts, since it is well known that with decreasing temperature only due to EPR absorption (absorption of Ni^{3+} and Ni^{2+} Ni^{2+}). The ions progressively reduce their intensity until it disappears at lower temperatures [33].

3.3.6 . Magnetic susceptibility measurements

To obtain additional information about the magnetic behavior of nickel-lead-borate glasses and glass-ceramics, magnetic susceptibility measurements were performed. Fig. 6 shows the temperature dependence of the inverse magnetic susceptibility of $xNi_2O_3(100-x)[3B_2O_3•PbO_2]$ samples with different nickel(III) oxide contents. Based on the EPR data presented above, we observe that the magnetic behavior of the nickel-lead-borate samples is due to the presence of magnetic Ni 2+ ions, since the host lead-borate glass matrix was found to be diamagnetic. [33]

The magnetic data presented in Fig.3.6. show that the magnetic susceptibility of the studied samples increases with increasing their Ni_2O_3 content . This can be correlated with the increase in the number of magnetic Ni^{2+} ions that appears with increasing Ni_2O_3 added to the lead-borate host matrix.

Using the experimental magnetic susceptibility data of the studied samples (Fig. 3.6), we determined several important magnetic parameters such as: the paramagnetic Curie temperature (θ_p), Curie constant (C) and effective magnetic moment on nickel ions (μ_{eff}). The values obtained for the above-mentioned parameters are listed in Table 3.1.

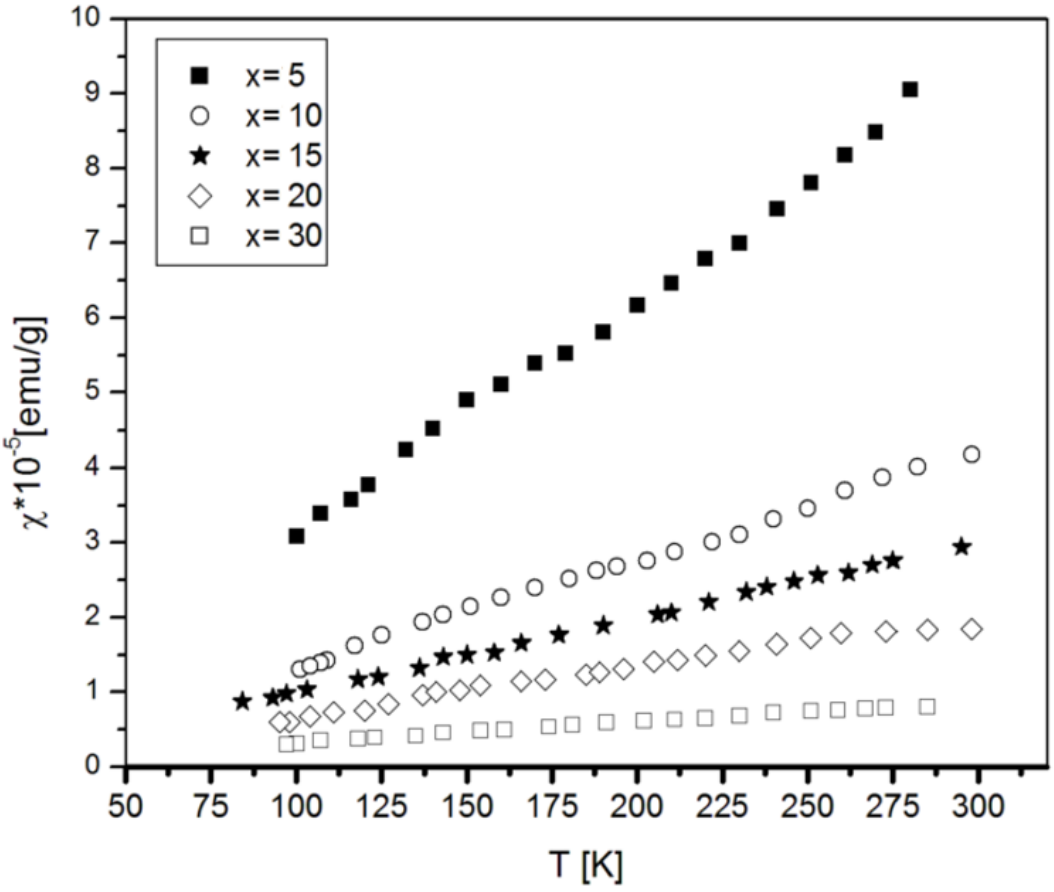

Fig.3.6. Temperature dependence of the mutual magnetic susceptibility of the system $xNi_2O_3 \cdot (100-x) \cdot [3B_2O_3 \cdot PbO_2]$ with x=5-30 mol% Ni_2O_3

3.3.7 . Adsorption of acetylene on the nickel-glass surface

The study on the adsorption of acetylene on the glassy powder sample with x = 20 mol% Ni_2O_3 was investigated by FTIR spectroscopy. The FTIR spectra of the sample with x=20mol% Ni_2O_3 recorded before and after the surface contact with C_2H_2 are represented in Fig. 3.8.

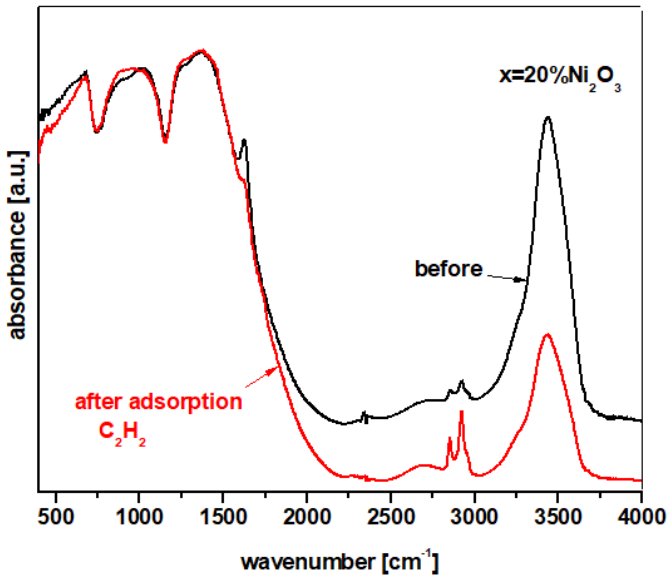

Fig. 3.8. FTIR spectra of the sample x=20 mol% Ni_2O_3 and of the sample surface in contact with C_2H_2.

After adsorption of acetylene on the glass surface, in the presence of water (IR bands located at approximately 1640 and 3430 cm^{-1}), acetylene was converted to acetaldehyde, CH_3CHO. The increase in intensity of the IR bands centered at approximately 645, 945, 1630, 2850 and 3430 cm^{-1} can be attributed to vibrations of acetaldehyde. Some of the acetaldehyde was converted by oxidation to acetic acid. The IR bands located at ~1025, ~1340, ~1375, ~1474, ~1535 and ~2925cm^{-1} can be attributed to adsorbed acetate groups. A mechanism can be proposed to explain the formation of acetaldehyde and acetic acid in the reaction of acetylene with water in the presence of O_2:

$$C_2H_2 + H_20 \rightarrow CH_3 - CH = O$$

$$CH_3 - CH=0 + 1/2O_2 \rightarrow CH_3 - COOH$$

CHAPTER 4. LEAD-BASED GLASS AND GLASS-CERAMICS IMPURIFIED WITH IRON OXIDE

4.3. Results and discussions

4.3.1. XRD diffraction

The XRD diffraction patterns of the synthesized samples $xFe_2O_3(100\text{-}x)[3B_2O_3 \cdot PbO_2]$ with x≤30mol% Fe_2O_3 shown in Fig. 4.1. do not show distinct diffraction peaks confirming the amorphous nature of these samples. In the sample with x =40% Fe203, the XRD patterns reveal two large halos with characteristic peaks assigned to the standard data of the rhombohedral crystalline phase α- Fe203

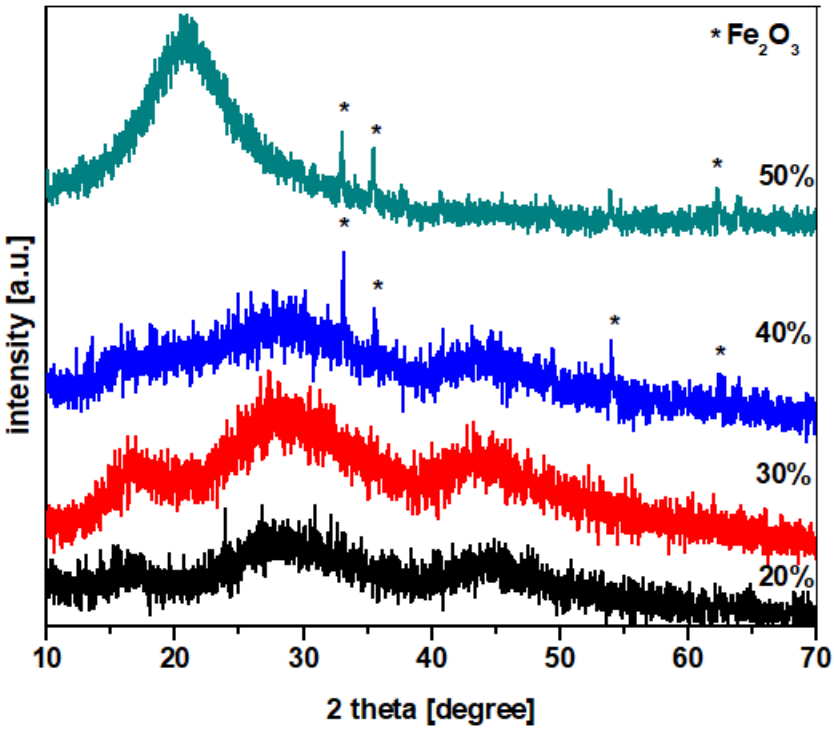

Fig.4.1. XRD patterns of the system $xFe_2O_3 \cdot (100\text{-}x)[3B_2O_3 \cdot PbO_2]$ where x=20-50 mol % Fe_2O_3.

The sample with x=50mol% Fe_2O_3 shows a broad peak centered around $2\theta = 21^0$ overlapping with the characteristic peaks corresponding to the crystalline α- Fe_2O_3 phase . The

presence of diffraction halos in the small angle range shows that the diffraction peak intensities characteristic of the crystalline α- Fe_2O_3 phase are low, suggesting either low crystallinity, low crystal size, or the presence of amorphous Fe_2O_3. Consequently, the small-sized α- Fe_2O_3 nanoparticles from the host matrix were successfully synthesized using the melt quenching method in the absence of any heat treatment.[80]

4.3.2. FTIR spectroscopy

Fig. 4.2. illustrates the FTIR spectra of iron-doped lead-borate glasses and glass-ceramics in the xFe2O3 system $\cdot_{(}$ 100 - x) [$3B_2O_3 \cdot PbO2_{]}$ with x= 5-50mol % Fe_2O_3 In the FTIR spectrum of Fe_2O_3, the bands located at approximately 470 and 510 cm^{-1} are assigned to Fe-O vibrations. The IR band located at approximately 580 cm^{-1} is associated with Fe-O vibrations in the [FeO_4] structural units .

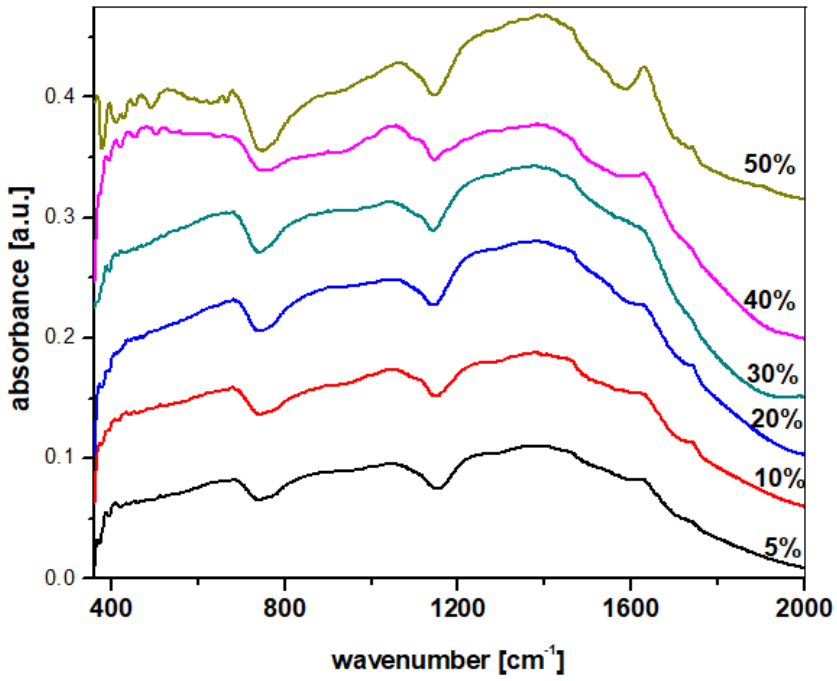

Fig.4.2. FTIR spectra of the system $xFe_2O_3 \cdot (100\text{-}x)[3B_2O_3 \cdot PbO_2]$ where x = 5-50mol% Fe_2O_3.

4. 3.3. UV-Vis spectroscopy

The UV-VIS absorption data of $xFe_2O_3\cdot(100-x)[3B_2O_3\cdot PbO_2]$ glasses and $Fe_2O_3\cdot(100-x)[3B_2O_3\cdot PbO_2]$ glass-ceramics with x=5-50mol% Fe_2O_3 are shown in Fig. 4.3. host.

Pb^{+2} with $6s^2$ electronic configuration absorbs strongly in the ultraviolet region with an absorption band centered at 310 nm due to the parity allowed $6s^2$-6sp transition [90].

Iron ions usually exist in glass as both Fe^{+2} ions in octahedral coordination and Fe^{+3} ions mainly in tetrahedral coordination, but some in an octahedral site. The Fe^{+2} ions have the 3d6 electronic configuration with a single allowed spin transition $_{t2g} \rightarrow {}_{eg}$ which is assigned to 970nm. The Fe^{+3} ion has the $3d^5$ configuration for which no spin-allowed transitions are possible and only weak bands can appear at a short wavelength corresponding to only a single spin-forbidden transition, such as the 325-520nm and 700nm region [91].

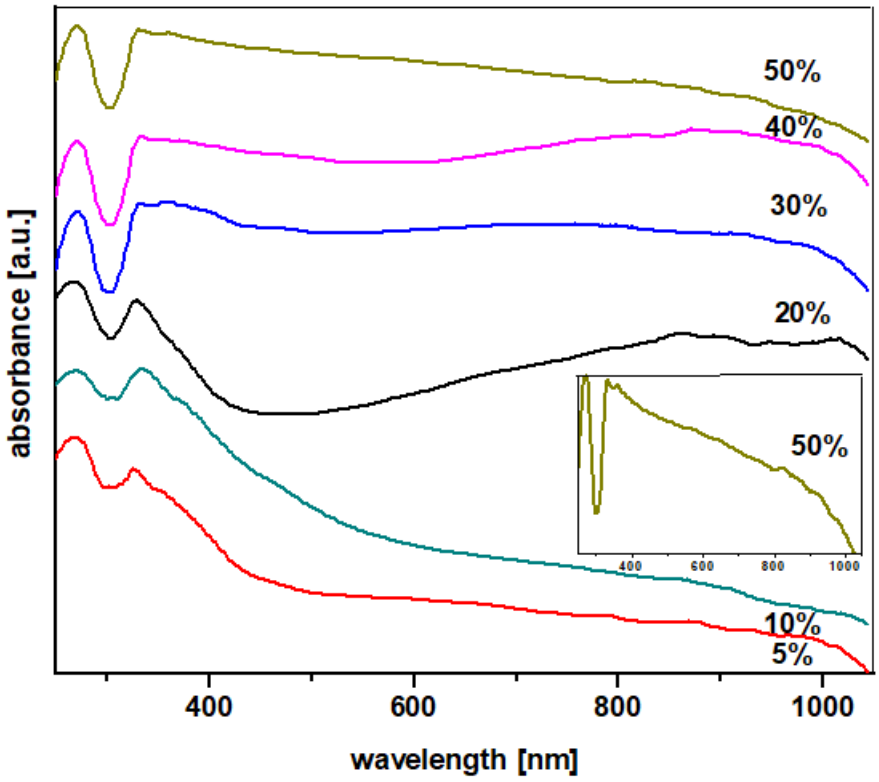

Fig.4.3. UV-VIS spectra of the system $xFe_2O_3\cdot(100-x)[3B_2O_3\cdot PbO_2]$

where x = 5-50mol % Fe_2O_3

4. 3.4. Optical gap energy

The direct and indirect gap energy, E_g can be calculated from the curves obtained from the UV-VIS absorption spectra, Fig. 4. 4a and 4.4b by plotting $(\alpha hv)^{1/2}$ and $(\alpha hv)^2$ respectively versus the photon energy, *hv* and extrapolating the linear part of the curves to meet *the hv axis* at $(\alpha hv)^{1/2} \rightarrow 0$ and $(\alpha hv)^2 \rightarrow 0$, respectively [22]. From Fig. 4.4c, it can be observed that the compositional evolution of the gap energy for both direct and indirect transitions decreases with increasing Fe_2O_3 content up to 50 mol%.

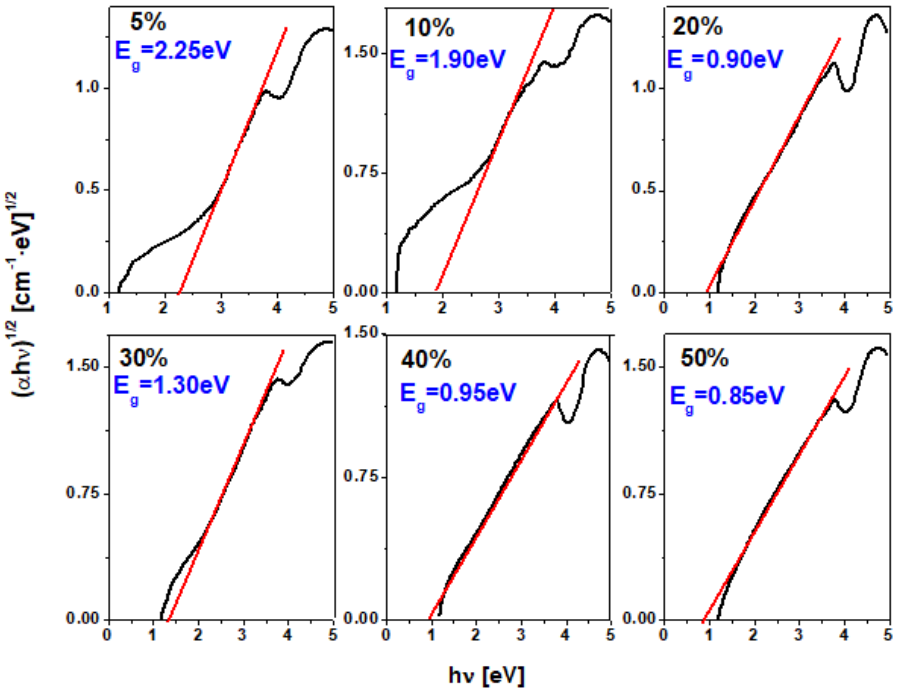

Fig.4.4.a Graphs of the system $(\alpha hv)^{1/2}$ and b) $(\alpha hv)^2$ versus *hv* for $xFe_2O_3 \cdot (100\text{-}x)[3B_2O_3 \cdot PbO_2]$ where x=5-50mol% Fe_2O_3

The values for the direct gap energy range gradually from 0.85 to 2.25eV, while for the indirect range, the values vary from 1.94 to 2.82eV with increasing content up to 50mol% Fe_2O_3 suggesting semiconductor behavior.

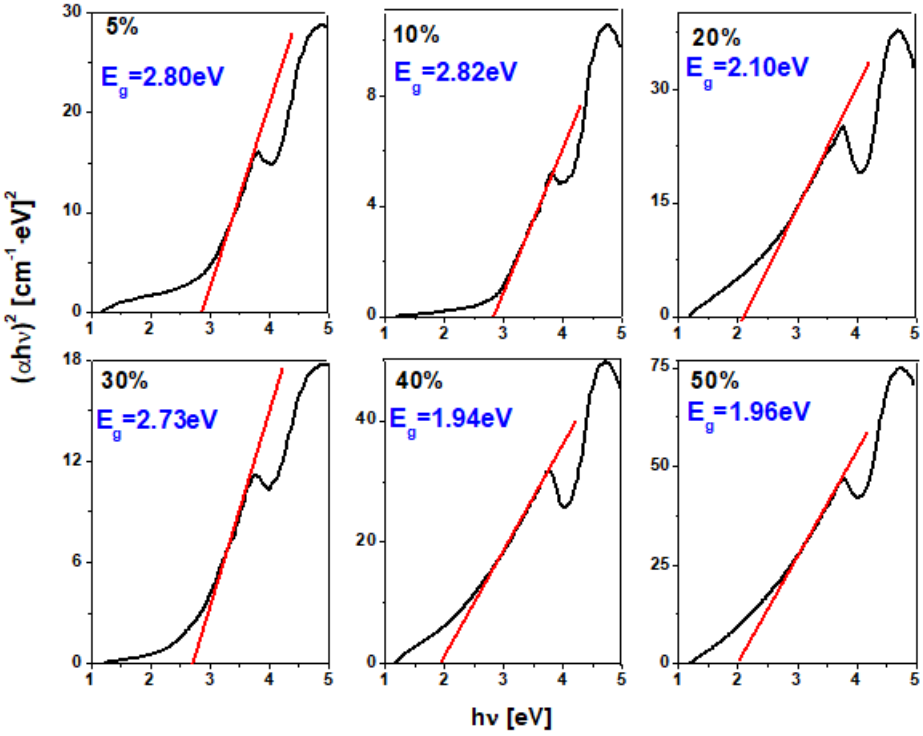

Fig.4.4.b Linear extrapolation of the optical range energy (E_g) of the system $xFe_2O_3 \cdot (100-x)[3B_2O_3 \cdot PbO_2]$ where x=5-50mol% Fe_2O_3

4.3.5. EPR spectroscopy

Fe^{+3} exhibits room temperature EPR resonance lines centered at approximately g~4.3 and 2. The resonance line located at approximately g~4.3 has been detailed for a variety of strongly distorted neighborhoods, such as the rhombic or tetragonal symmetries of isolated Fe^{+3} ions [89]. The signal located at approximately g~4.3 is assigned to Fe^{+3} as a lattice former, while the resonance line centered at approximately g~2 is assigned to octahedral Fe^{+3} ions as a lattice modifier.

The resonance line located at approximately g~2 has been attributed to Fe^{+3} ions arranged in octahedral symmetry sites, with low crystal fields, or associated in magnetic clusters. Fe^{+2} species are also present along with Fe^{+3} ions, but are EPR silent at room temperature.[95]

The intensity of the resonance line located at approximately g~2 decreases strongly with increasing Fe_2O_3 content up to 50 mol% Fe_2O_3. This decrease is due to the destruction of the configuration in the vicinity of the iron ions located in magnetic clusters and/or the conversion of Fe^{+3} to Fe^{+2} ions. On the other hand, the decrease in the line width with increasing iron oxide

content shows that the dipolar interactions between the iron ions responsible for this line decrease. In this case, Fe(III) located in an octahedral site surrounded by negatively charged oxygen coming from the nearby [PbO4] or/and [BO4] tetrahedral units , in agreement with IR data.

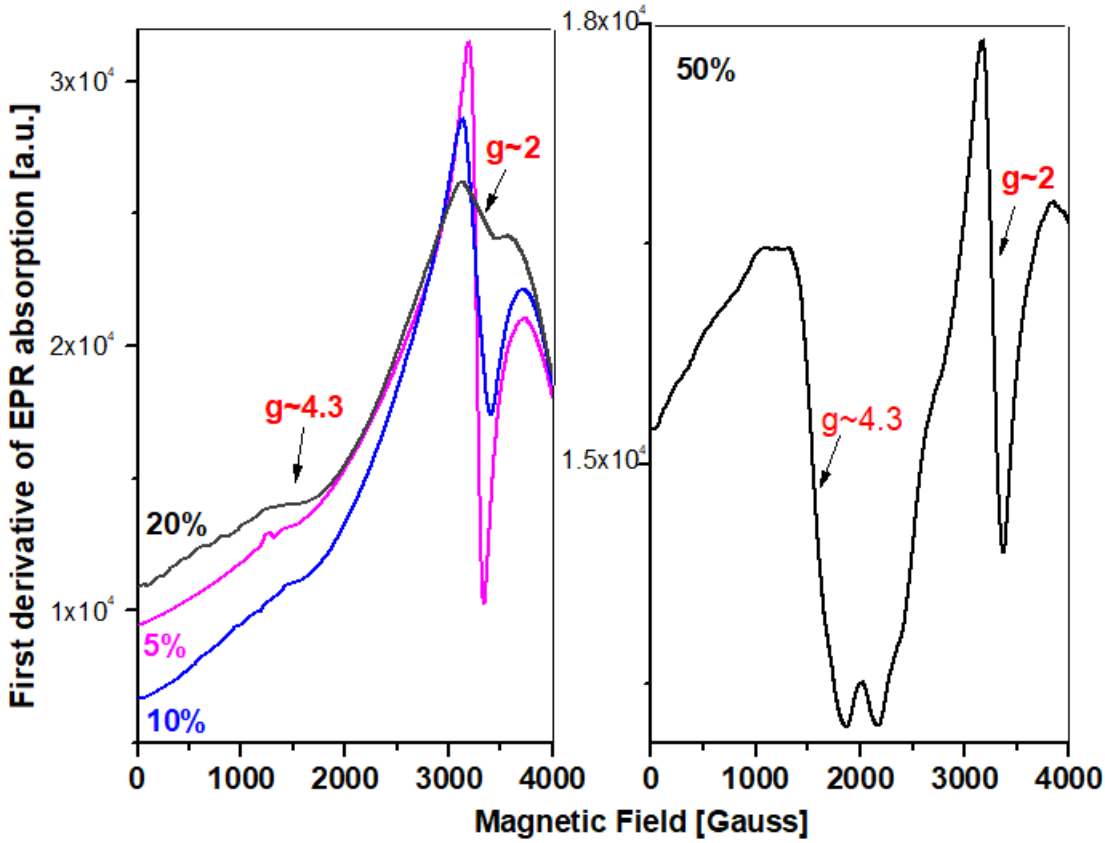

Fig.4.5. EPR spectra of the system $xFe_2O_3 \cdot (100-x)[3B_2O_3 \cdot PbO_2]$

where x =5, 10, 20 and 50 mol % Fe_2O_3

The intensity and width of the resonance line located at about g~4.3 gradually increases with the iron(III) oxide content up to 50 mol% Fe_2O_3. This structural evolution can be explained by considering that Fe(III) replaces the lead and/or boron atoms covalently bonded to four oxygen atoms in a distorted tetrahedron. The [FeO_4] tetrahedra require charge compensation as a network former, for example, by lead cations disrupting the tetrahedral symmetry.

Consequently, Fe(III) ions involving randomly distorted units have the ability to impose a certain order in its vicinity and to produce the destruction of the configuration in the vicinity of iron ions.[97-100]

4. 3.6. Acetylene adsorption Molecules on the surface of the samples

Transition metals, as well as their oxides, sulfides, and carbides, are unique in their ability to catalyze chemical reactions, primarily due to the multiplicity of low-energy surface electronic states that can readily donate and/or accept electrons in the process of bond formation and bond breaking. Transition metal oxides are widely used as catalysts in the petroleum, chemical, and environmental industries as heterogeneous catalysts and catalytic supports [90].

We studied the adsorption of acetylene, C_2H_2 on powder samples with x = 20 and 40 mol % Fe_2O_3.

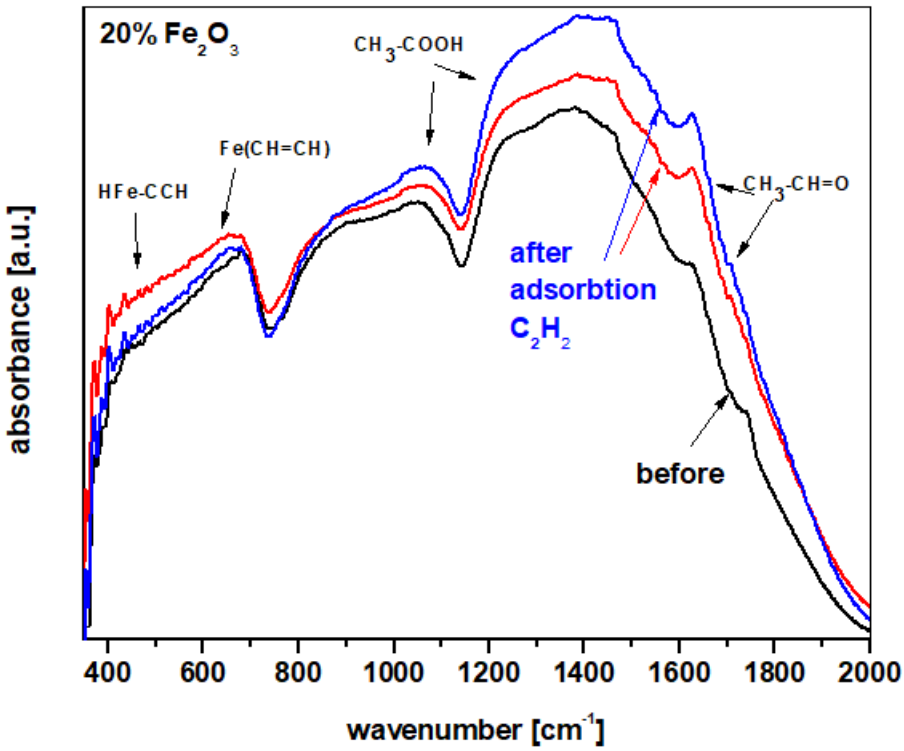

Fig.4.6.a FTIR spectra of samples with x=20 mol% Fe_2O_3 and a sample surface in contact with C_2H_2

Fig. 4.6. shows comparative IR spectra of the samples and a surface of the samples in contact with C_2H_2. A simple inspection of the IR data suggests that the structure of the samples was successfully modified by adsorption of C_2H_2. The adsorption of acetylene on glass and glass-

ceramic surfaces demonstrates that these materials have a band edge position suitable for photocatalytic reactions of a large number of organic molecules [101-103]

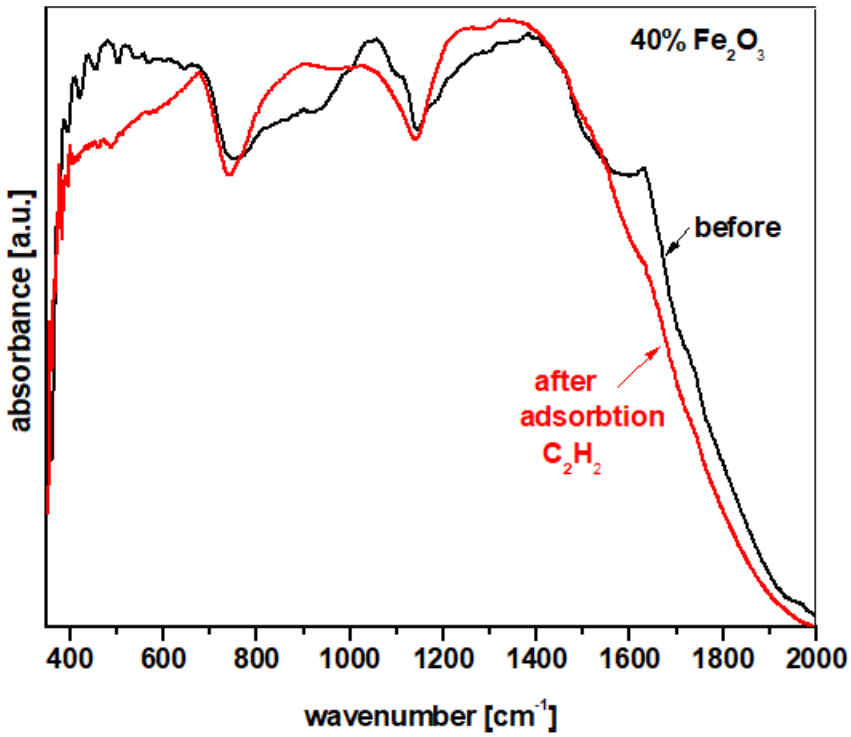

Fig.4.6.b FTIR spectra of samples with x=40 mol% Fe_2O_3 and a sample surface in contact with C_2H_2

For the sample with x=20mol% Fe_2O_3 some changes occur in the FTIR spectra after C_2H_2 adsorption . The new IR bands centered at approximately 655, 760, 1385, and 1960 cm^{-1} can be attributed to acetylene vibrations [27]. The IR peaks located at approximately 1660 and 1710 cm^{-1} are characteristic absorptions of the carbonyl stretch. In the presence of water, some of the surface acetylene is converted to acetaldehyde, CH_3CHO .[80] After C_2H_2 adsorption , the increase in the intensity of the IR bands centered at approximately 1067 and in the region between 1165 and 1800 cm^{-1} can be due to acetic acid vibrations [26]. A mechanism for the observed products can be proposed as follows:

$$C_2H_2 + H_2O \rightarrow CH_3 - CH = O$$

$$CH_3 - CH=O + 1/2O_2 \rightarrow CH_3 - COOH$$

The π system of acetylene can react directly with iron metal, yielding a wide range of acetylene complexes. The presence of IR bands located at approximately 470, 668, 1754 and 1976 cm^{-1} is attributed to vibrations in the HFe-C≡CH complexes. Then, absorption bands centered at approximately 677, 700, 876 and 1540 cm^{-1} are attributed to vibrations in Fe(CH=CH) [92]. These π products are the most common in transition metal reactions. Subsequent rearrangements after the initial coordination vary depending on the electron pair acceptor, leading to its characteristic products.[104]

4.4. Conclusions

Glass and glass ceramics of the system, $xFe_2O_3(100-x)[3B_2O_3 \cdot PbO_2]$ were synthesized in the interval of composition $5 \leq x \leq 50$mol % Fe_2O_3. XRD analysis reveals that increasing the Fe_2O_3 content above 30 mol% determines the development of the α-Fe_2O_3 crystalline phase in the host matrix.

IR data show that increasing the Fe_2O_3 content causes unit conversions structural units $[BO4] \rightarrow [BO3]$ and $[PbO4] \rightarrow [PbO3]$. The excess oxygen ions will be accommodated in the matrix by forming structural units $[FeO_n]$ with n=4 and 6.

The broadening of the UV-VIS bands located in the regions between 295 and 1050 nm when the concentration of Fe_2O_3 increases in the lattice matrix by up to 30 mol% suggests their applications as solar cells.

The EPR spectra of Fe^{+3} ions show two well-defined lines at effective g values of g~4.3 and g~2.0 which are considered as the signature of their presence in a glass and glass-ceramic host matrix. The intensity of the resonance lines depends on the concentration of Fe_2O_3 in the host matrix.

CHAPTER 5. PALLADIUM-DOPED LEAD-BASE GLASS AND GLASS-CERAMICS

5.3. Results and discussions

5.3.1. XRD diffraction

X-ray diffraction patterns of the system xPd•(100-x) [$3B_2O_3$•PbO_2] where x= 20-40% mol Pd are shown in Fig. 5.1. They indicate two broad halos characteristic of the amorphous structure.

Photoemissions from the Pd (3d) ground state have been observed in the X-ray diffraction spectrum. Several peaks are found for the immobilized palladium states.[109]

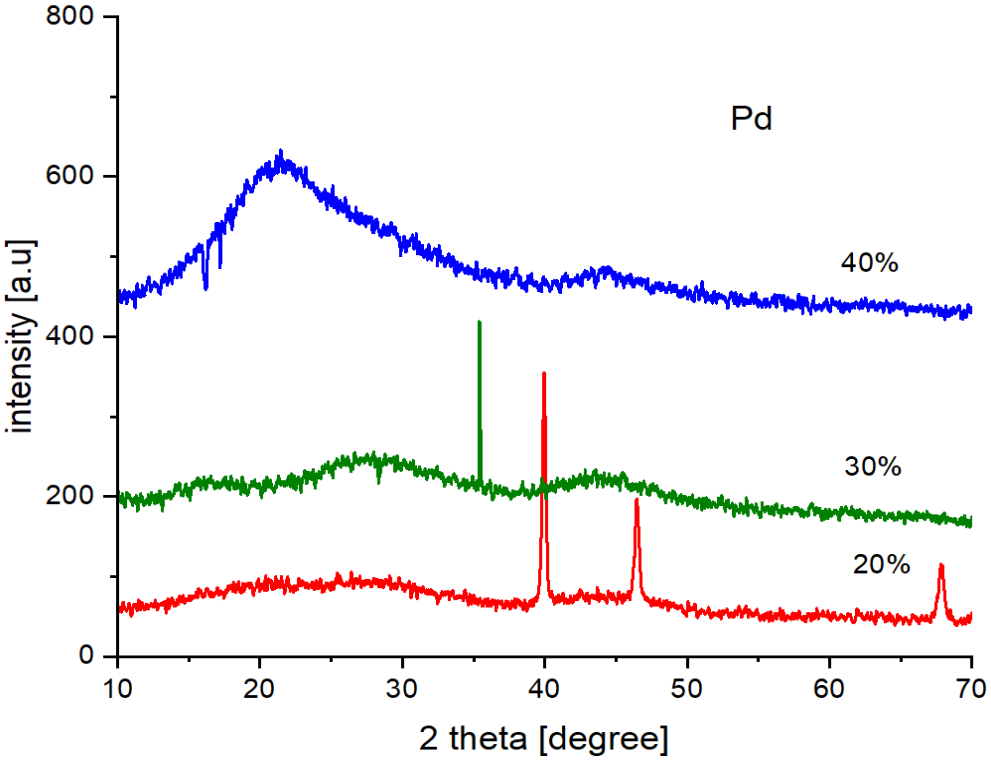

Fig.5.1 XRD diffractograms of the xPd•(100-x) [$3B_2O_3$•PbO_2] system where x= 20-40 mol% Pd

5.3.2. FTIR spectroscopy

Fig.5.2. illustrates the FTIR spectra of lead borate glasses doped with palladium and aluminum oxide and glass-ceramics in the system xPd•(100-x) [$3B_2O_3$•PbO_2] where x= 5-40% mol Pd .

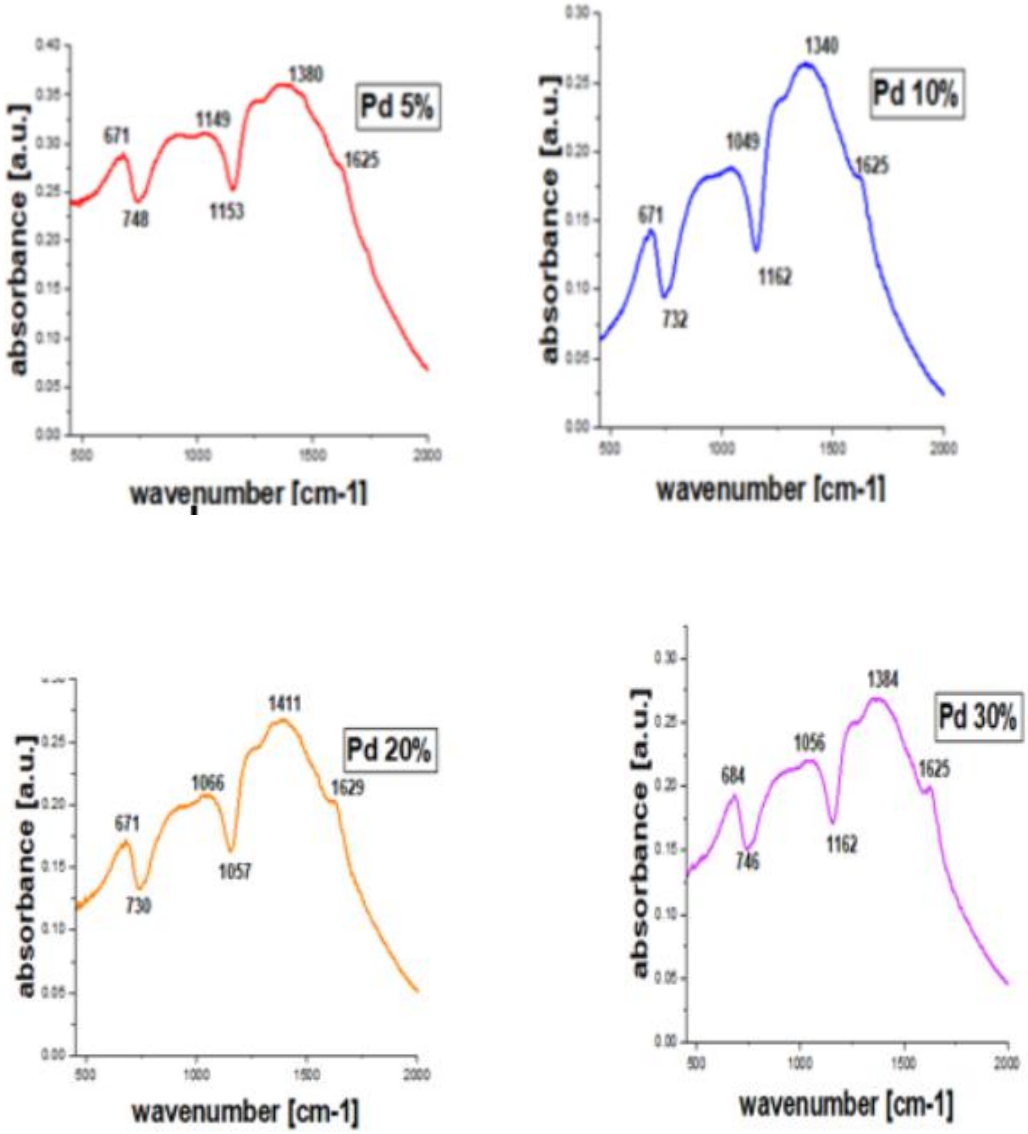

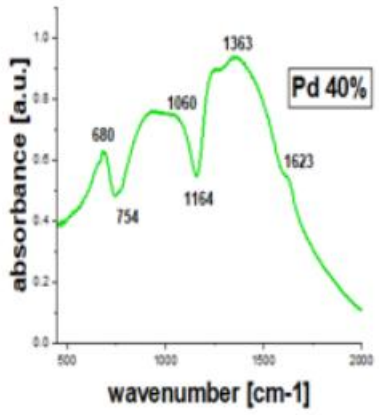

Fig. 5.2. FTIR spectra of the system xPd•(100-x) [3B $_2$ O $_3$ •PbO $_2$] where x= 5-50% mol Pd

For the bands in the IR spectrum at x= 5-20% it decreases from 1380 cm $^{-1}$ to 1066 cm $^{-1}$ due to the glassy spectrum of B $_2$ O $_3$ and is attributed to the B-O-B stretching vibration of the [BO $_4$] group. It is observed that with increasing concentration this band decreases from 1380 cm $^{-1}$ to 1164 cm $^{-1}$.

The existence of a shoulder at 1625 cm $^{-1}$ that remains constant is attributed to some palladium species: Pd $_2$, Pd $_3$, Pd $_4$ **,** Pd $_5$ and Pd $_6$ that remain constant throughout the impurity at 1623 cm $^{-1}$.[62-64]

5.3.3. UV-VIS spectroscopy

The UV-Vis absorption data of glasses with the composition xPd •(100-x)[3B$_2$O $_3$•PbO $_2$] where x= 5-40 mol% Pd are presented in figure 5.3.

A simple inspection of the spectrum (fig.5.3.) suggests structural changes in the UV-VIS bands indicating that the lead ions occupy different local sites in the host matrix. By increasing the lead content and up to 20% palladium ions in the host matrix, the absorption band edge gradually shifts towards higher wavelengths, then increasing the palladium content implies a decreasing trend towards lower wavelengths.

The most important UV-VIS bands are: the band located between 250 nm and 295 nm originating from the host glassy matrix, another band in the ultraviolet region is the one located at 300 nm and the last wavelength is the one located between 300 nm and 34 0 nm .

The intensity of the first UV-VIS absorption band remains almost unchanged by increasing the lead content up to 30 mol% Pd, after which it gradually decreases.

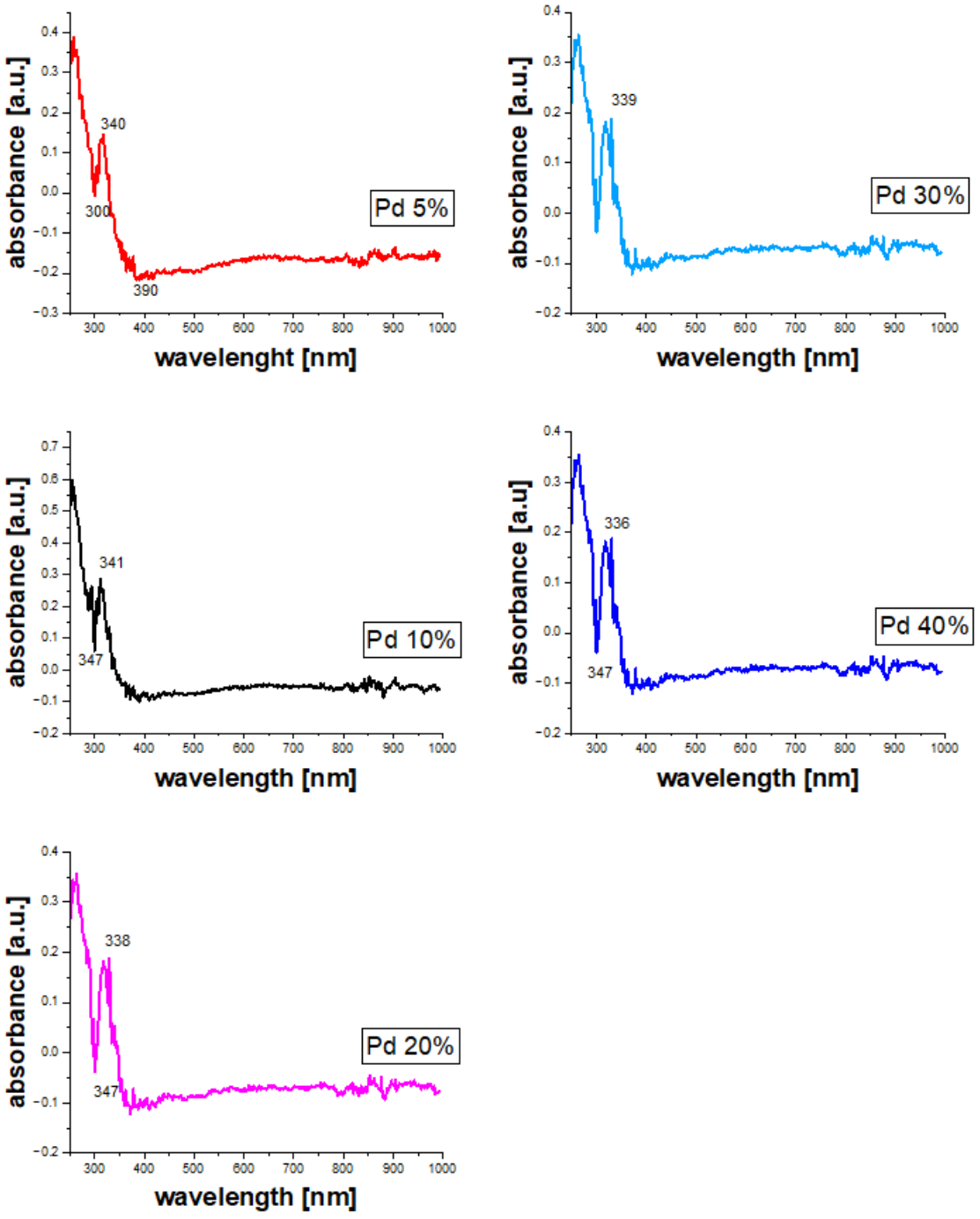

Fig. 5.3 UV-VIS spectra of the system xPd•(100-x) [3B $_2$ O $_3$ •PbO $_2$] where x= 5-40% mol Pd

5.3.5. Adsorption of acetylene molecules on the surface of samples

The main industrial use of carbide is to obtain acetylene, by reacting it with water (carbide = calcium acetylide reacting with water produces acetylene and calcium hydroxide):

$$CaC_2 + 2H_2O \rightarrow CH \equiv CH + Ca(OH)_2 \downarrow$$

In the presence of palladium Pd or $Pd^{+2,}$ ethene is formed:

$$CH \equiv CH + H_2 \rightarrow CH_2 = CH_2$$

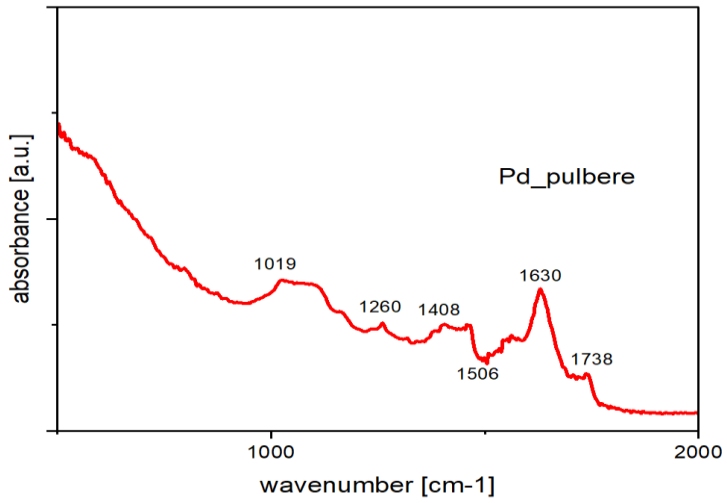

Fig. 5.5.a) FTIR spectra of the xPd•(100-x) [$3B_2O_3$•PbO_2] system sample with Pd powder, before adsorption

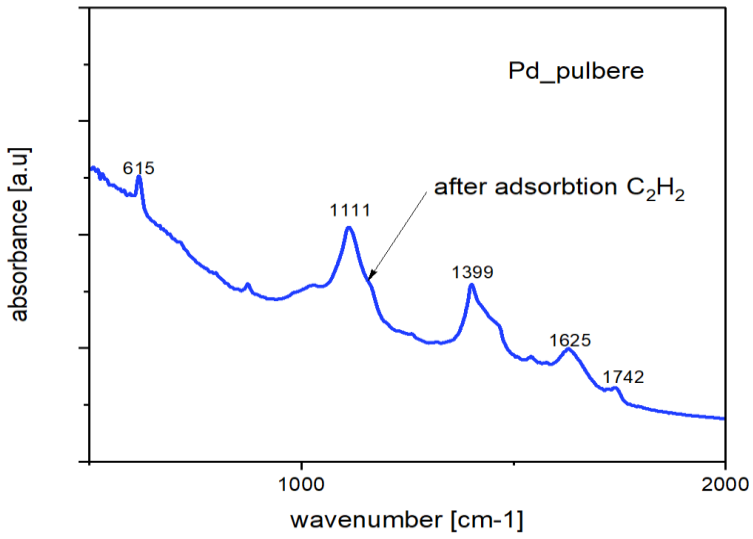

Fig. 5.5.b) FTIR spectra of the sample of the system xPd•(100-x) [$3B_2O_3$•PbO_2] with Pd powder, after adsorption

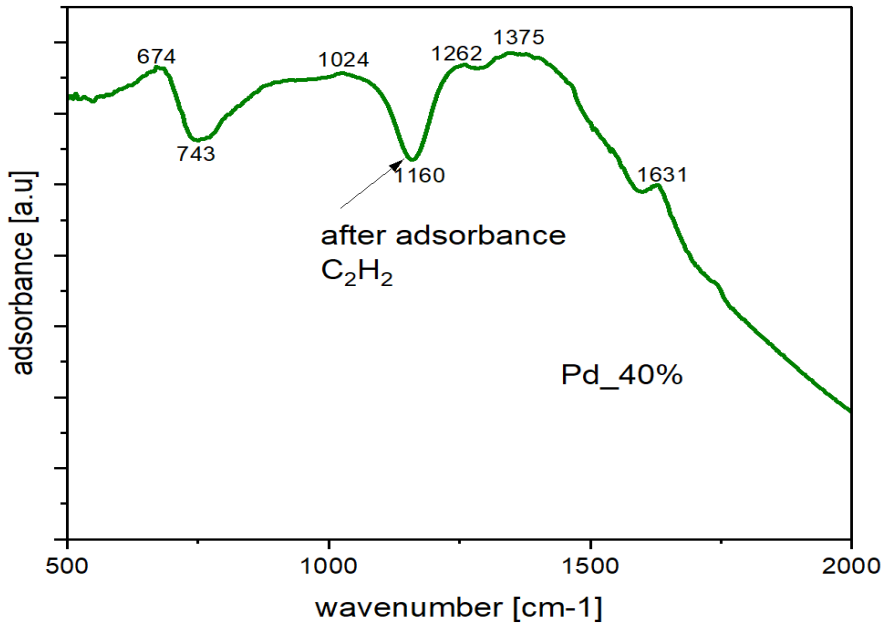

Fig. 5.5.c) FTIR spectra of the xPd•(100-x) [3B $_2$ O $_3$ •PbO $_2$] system sample with x= 40% mol Pd, after adsorption

5.3.6.Molecular modeling

5.3.6.1.Introduction

Investigations on the adsorption of ethylene have been carried out on metal surfaces. When ethylene is adsorbed on a metal surface, C $_2$ H $_4$ undergoes hydrogenation and dehydrogenation processes. Ethylene can be molecularly adsorbed on a metal surface in two ways:

a. π , if ethylene interacts with a single metal atom;

b. di-σ, if ethylene interacts with two metal atoms.

In the calculations performed, adsorption verifies the Pauli principle, according to which there cannot be two electrons with the same configuration, there being a Coulomb interaction of attraction between two electrons, or repulsion between four electrons.

We have performed a DFT study of the interaction of ethylene with a palladium surface, in which 1-6 Pd atoms are present in the cluster, the two types of adsorption π and di –σ being present in the analysis. The activation of the C-H bond of ethylene is analyzed with respect to

either one Pd atom or two Pd atoms. A primary aspect of the calculations is the geometric optimization of ethylene, C_2H_4 with respect to the clusters, Pd_n. The advantage is that the interaction between ethylene and the cluster can be highlighted by calculations, which describe the molecular properties of the cluster, the adsorption and the activation of the C-H bond by one or more palladium atoms.

5.3.6.2. Calculation method

The DFT (Density Functional Theory) method is used to determine the geometries of adsorption energies and transition states for $C_2H_4 – Pd_n$ systems , with n=1-6 palladium atoms. The Gaussian program, applied at Babeş-Bolyai University, Cluj-Napoca, Faculty of Physics, has the possibility of representing molecular orbitals resulting from linear combinations of Slater orbital types and solving the Khon-Sham equation. [116]

The adsorption energies were calculated with the expression:

$$E_{ads} = E_{C_2H_4/Pd_n} - (E_{Pd_n} - E_{C_2H_4})$$

where E_{Pdn} – is the energy of the cluster Pd_n and $E_{C_2H_4}$ the energy of ethylene, and $E_{C_2H_4/Pd_n}$ the total energy of the impurity cluster of the adsorbent system. The system will be stable if the adsorption energy E_{ads} it is negative.

5.3.6.3. Clusters Pd_n, n= 1-6

3.a. For a single palladium atom, the degeneracy between the lowest series of the palladium atom, from the d^9 to $\rightarrow d^{10}$ level, was calculated to be 26 kmol/mol.

3.b. For two palladium atoms the calculations to determine the singlet and triplet states for the two palladium atoms are slightly different. In the singlet case, with the Pd-Pd atom distance of 2.74 Å, the binding energy is -25 kmol/mol, at the vibration frequency of 187 cm^{-1} , and for the triplet, with the Pd-Pd atom distance of 2.56 Å, the binding energy is -29 kmol/mol, at the vibration frequency of 213 cm^{-1} . The triplet state is more stable by 4 kmol/mol , the Pd-Pd bond length is shorter and the vibration frequency is higher.

3.c. For n=3 , Pd_3 the triangular geometry D_{3h} is more stable than the linear one $D_{\infty h}$. Small cluster analysis shows that compact structures are more stable than open structures, so that

triplet spin states are more stable than singlet spin states. Cluster geometries depend on the cluster size and on structure determinations obtained by different methods.

3.d . For n=4, Pd_4 these clusters present spin and triplet ground states. The strength of the Pd-Pd bond decreases with cluster size. The energy band calculation for the Pd structure is 0.37 electrons per s orbital and 9.63 electrons per d orbital. The Mulliken populations show a decrease in electrons from the s shell to the d shell.

3.e . In the $Pd(C_2H_4)$ cluster, electron donation and acceptance processes occur due to the interaction of ethylene with the transition metal. Donation involves a transfer of electrons from the πethylene orbital to the unoccupied metal orbitals, while electron acceptance populates the ethylene π orbital with electrons from the unoccupied metal orbital. Both electron donation and acceptance are attractive interactions. The Pauli-type repulsion is due to the interaction between the occupied orbitals of ethylene and the transition metal. The first consequence of the donation and acceptance processes is the weakening of the CC bond. The CC bond length increases from 1.34 Å in the gas phase to 1.4 Å in the complex.[117]

The formation of Pd-C bonds produces a small hybridization of the carbon atom from sp^2 to sp^3. The dihedral angle between the HCC and the CC-Pd plane increases from 90° to 98°. For complete sp^3 hybridization this angle must be 120°. The ground state of the complex is singlet with a binding energy of -39 kcal/mol. For ethylene the total charge transfer is an acceptance of 0.07 electrons, and the donation to the metal is less than 0.01 electrons. [118]

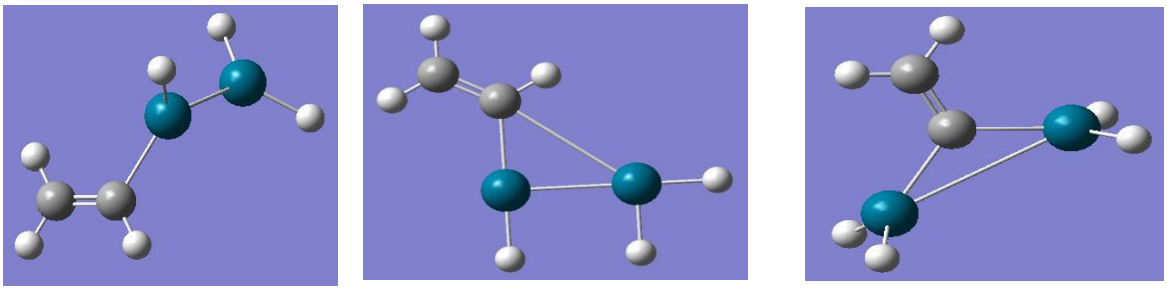

Fig. 5.3.7 Different transition states for CH bond activation for Pd_2 a)end -on b)side –on perpendicular c)side-on parallel

Indeed, the Pd -C_2H_4 – π complex is more stable at -39 kcal/mol than the free molecules in the ground states, while Pd_2 - C_2H_4 –π is more stable at -23 kcal/mol. Three transition states were investigated (Fig.5.3.7). In the end-on approach, the Pd-Pd axis is perpendicular to the CH

bond and only one Pd atom is involved in the interaction. The other Pd atom is kept at a distance from the ethylene.

5.3.6.5. Adsorption of ethylene on Pd clusters (n=3-6)

Ethylene adsorption on Pd_n clusters (n=3-6) was studied for the two adsorption modes π and di-σ. It was surprisingly found that the structure of the cluster associated with the di-σ adsorption mode changes. For Pd_n clusters (n=3-6), the bond between the two Pd atoms involved in the absorption is broken, fig. 5.3.8. Ethylene induces a reconstruction of the cluster: from the triangle to the linear Pd_3 structure and from the tetrahedron to the planar Pd_1 structure . Similar effects were suggested by Panks and others for the adsorption of H_2 on metal surfaces[116-120]

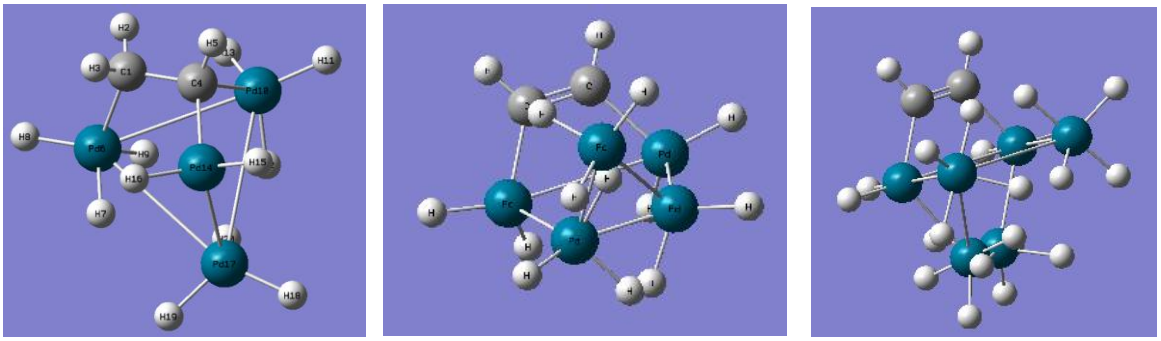

Fig. 5.3.8. Distorted clusters Pd4 (a), Pd5(b), Pd6(c) in di-σ-type adsorption of ethylene

In fig. 5.3.8. it is observed that the Pd-Pd distance decreases with the cluster size. Therefore, this effect of decreasing the distance between the Pd atoms will correspond to a total relaxation of the surface. The structural effect associated with the π adsorption mode is smaller and determines an increase in the bond length between the atom involved in the adsorption and the nearest neighbor. In the case of adsorption on a transition metal surface there is a tendency for the metal atoms involved in the adsorption to be pushed out of the surface.

For the distortion of adsorbed ethylene we found the same orientation as for the dimer, but a higher distortion, of the rehybridization type for the di-σ adsorption mode. The CC bond length is longer and is of the di-σ type. Tab.5.3.10 presents the spin state of the complexes, $C_2H_2Pd_n$. In di-σ adsorption, the reaction between ethylene and the cluster can be described as an additive

oxidation reaction in which the π bond of ethylene is broken and σ bonds between two Pd atoms and the carbon atom are formed. Therefore, the di-σ complexes are of the singlet type except for the $C_2H_2Pd_6$ complex where the ethylene distortion is lower. The ethylene distortion is lower in π adsorption, where the cluster spin is not perturbed.

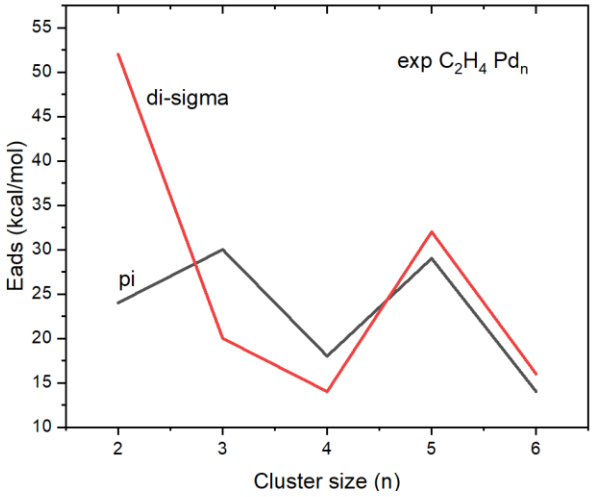

Fig.5.3.9 Ethylene π and di –σ adsorption energy for clusters, $C_2H_2Pd_n$

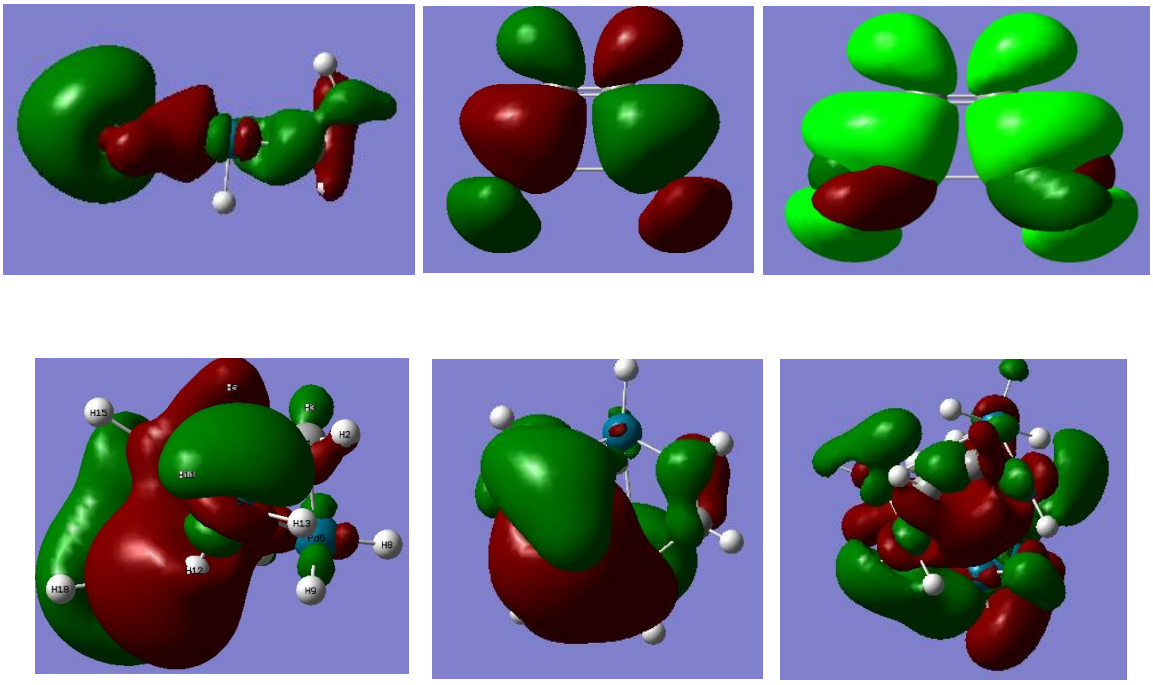

Fig.5.3.10. Energy surfaces, HOMO type for $C_2H_2Pd_n$ clusters , n=1-6

CHAPTER 6. LEAD-BASE GLASS AND GLASS-CERAMICS DOPED WITH ALUMINUM OXIDE AND PALLADIUM

6.3. Results and discussions

6.3.1. XRD diffraction

X-ray scattering diffractograms of the system xPd_Al $_2$O $_3$•(100-x) [3B $_2$O $_3$•PbO $_2$] where x= 30-50% mol Al $_2$O $_3$ are shown in Fig.6.1. indicate two broad halos characteristic of the amorphous structure. The X-ray diffraction patterns show the same symmetry of the initial lattice. When palladium is doped in the porous glass, the peaks are placed at greater distances.

The oxidation of palladium causes the shift of the X-ray lines, Kα1 - shifts observed in the samples with x= 30% and x=50%. One cause would be the effect produced by the simultaneous involvement of the 4d and 5s electrons in the chemical bond.

Since the energy of the X-ray line is the difference in energies of the corresponding levels E(Kα1)=E(1s)-E(2p $_{5/2}$). In Fig. 6.1 it is found that the displacement of the X-ray produces changes in the internal electronic energy levels.

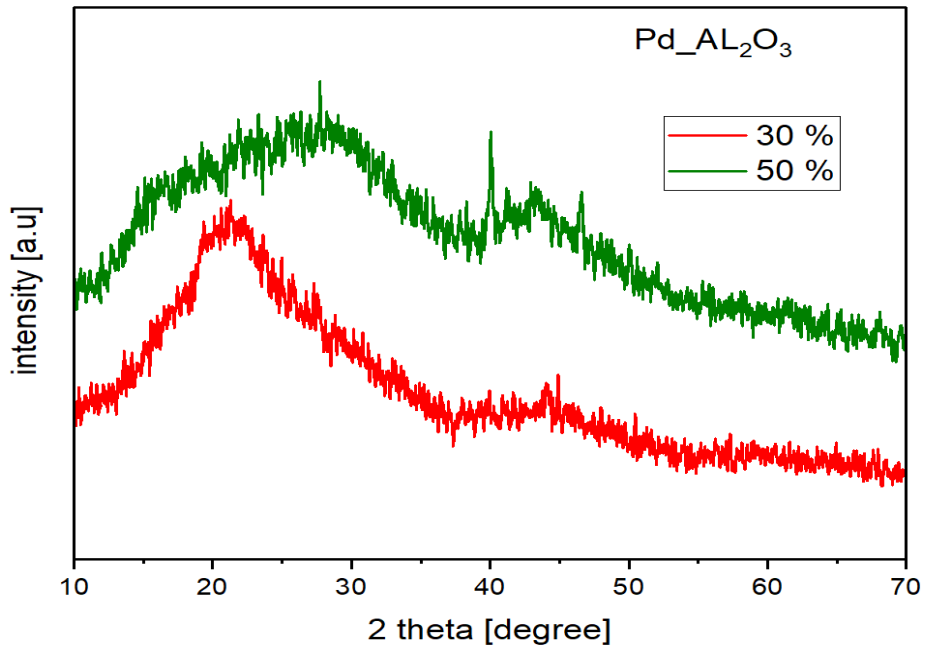

Fig.6.1 XRD diffractograms of the system xPd_Al $_2$O $_3$•(100-x) [3B $_2$O $_3$•PbO $_2$] where x= 30-50 mol% Al $_2$O $_3$

In tab. 6.1. d - the distance between the planes of the system network was calculated xPd_Al_2O_3•(100-x) [$3B_2O_3$•PbO_2] where x= 30% mol Al_2O_3 using the Origin 2025 program, by the interpolation method, using the Braag diffraction law, where n=1 and ƛ =1.504 Å:

6.3.2. FTIR spectroscopy

Fig.6.2. illustrates the FTIR spectra of lead borate glasses doped with palladium and aluminum oxide and glass-ceramics in the system xPd_Al_2O_3•(100-x) [$3B_2O_3$•PbO_2] where x= 5-50% mol Al_2O_3.

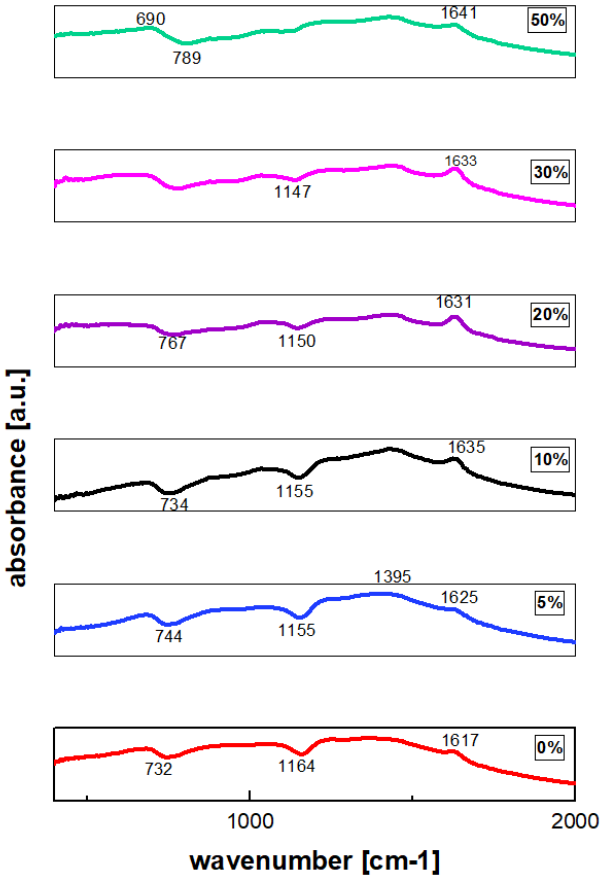

Fig. 6.2 FTIR spectra of the system xPd_Al_2O_3•(100-x) [$3B_2O_3$•PbO_2] where x= 5-50% mol Al_2O_3

For the spectra with x=5-50% a band at 1050 cm $^{-1}$ is observed which is attributed to the stretching vibration of the BO bond in the groups in which the B atom is tetra-coordinated. For x=50% the band at 1050 cm $^{-1}$ shifts to 1150 cm $^{-1}$, a shift due to the influence of aluminum on the BO bond in the [BO_4] units.

For the spectra with x = 10% a band is observed at 1200 cm $^{-1}$, in the spectrum with x= 30% it moves to 1255 cm $^{-1}$ presenting a shoulder at 1205 cm $^{-1}$. This band appears in the vitreous B_2O_3 spectrum at 1225 cm $^{-1}$ and is attributed to the stretching vibration of the B-O-B bond in groups in which boron is tri-coordinated, [BO_3]. For aluminum concentration x= 50% the intensity of the band at 1220 cm $^{-1}$ is higher than that at x=30%, so at high concentrations of aluminum oxide tri-coordinated boron atoms predominate, [BO_3].

Samples doped with alumina with a concentration of x=5-40% produce large changes present in the graphs. For example, the band at 1555 cm $^{-1}$ disappears, which proves the absence of the Al-OH bond.

The low-energy bands shift to high-energy ones: 892, 622 and 490 cm $^{-1}$, this shift being produced by a strong Al-O bond corresponding to high stability, when the glasses are doped with aluminum.[123]

6.3.3. UV-Vis spectroscopy

UV-Vis absorption data of glasses with the composition xPd_Al_2O_3•(100-x) [3B_2O_3 •PbO_2] where x= 5-50% mol Al_2O_3 are shown in Figure 6.4. The band located at ~300 nm is attributed to Pb^{+2} ions .

By increasing the palladium ion content up to 30 mol%, the intensity of this band increases.

With the increase of the aluminum oxide content in the host matrix, a gradual shift of the UV-VIS absorption bands located in the region between 340 nm and 450 nm towards longer wavelengths is observed, suggesting an increase in the number of unbound oxygen atoms in the host matrix. A possible explanation for this behavior is that lead ions are incorporated into the host matrix structure as network formers through the [PbO_4] and [PbO_3] structural units. Then, by

increasing the high concentrations of aluminum oxide, they behave as network modifiers and as a result, the network continuity is interrupted and a large number of unbound oxygen atoms are formed.

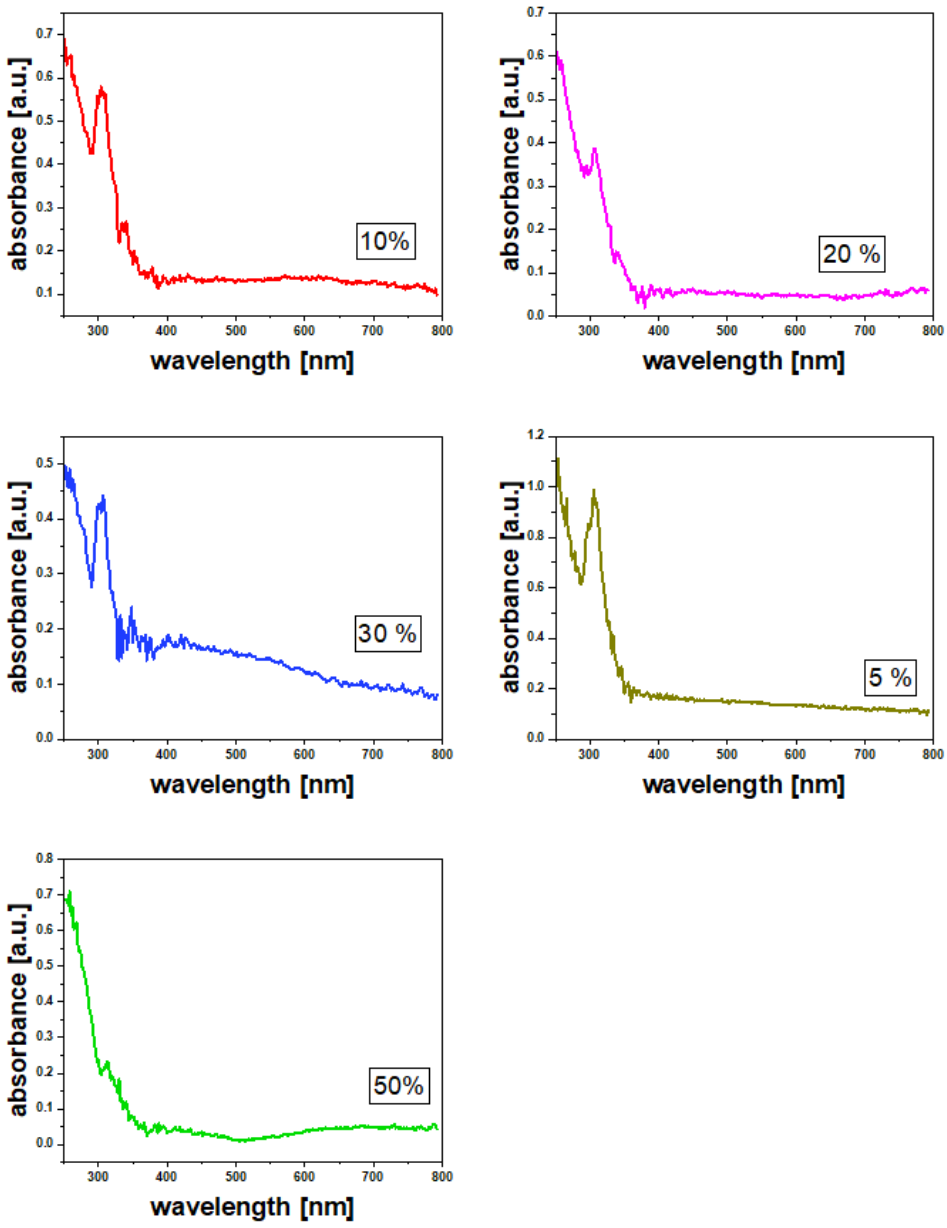

Fig. 6.3 UV-VIS spectra of the system xPd_Al $_2$O $_3$•(100-x) [3B $_2$O $_3$•PbO $_2$] where x= 5-50% mol Al $_2$O $_3$

CHAPTER 7. GENERAL CONCLUSIONS

The bottles of nickel-lead-borate and glass-ceramics with the composition $xNi_2O_3(100-x)[3B_2O_3 \cdot PbO_2]$ in which x=0-50 mol% Ni_2O_3 were synthesized by the melt quenching method. The obtained samples were investigated by XRD, FTIR, UV-Vis and EPR spectroscopy and magnetic susceptibility measurements.

IR analysis indicates the gradual transformation of nickel ions from tetrahedral to octahedral sites and the formation of orthoborate structural units by increasing the content of Ni_2O_3 of the samples.

UV-VIS optical absorption spectra of nickel-lead-borate systems reveal broad and strong bands due to nickel ions in the range of 375 - 1000 nm . The changes in the optical gap energy value with increasing Ni_2O_3 content can be understood from the point of view of the structural changes that occur in the glasses and glass-ceramics studied.

The EPR spectra obtained for nickel-lead-borate glass/glass-ceramics show two broad resonance lines, one located at g≈2.21 due to Ni^{2+} ions, the other located at g≈8 due to blocked nickel clusters. Their intensity and line width depend on the Ni_2O_3 content of the samples. The intensity of the resonance lines decreases with decreasing temperature.

The effective magnetic moments of the nickel-lead-borate glasses were found to be in the range between 3.27 and 3.44 μ_B. The large value of the magnetic moment of the x=30% Ni_2O_3 sample, $\mu_{eff} = 4.32\ \mu_B$, suggests the presence of a strong antiferromagnetic interactions in the host lattice due to the formation of crystalline NiO and $Ni_6B_2O_6$ phases . EPR and magnetic susceptibility data suggest a superparamagnetic behavior of nickel-lead-borate glass-ceramics with $x \geq 30$ mol% Ni_2O_3.

Glasses and glass-ceramics of the system $xFe203 \cdot (100-x)[3B_2O_3 \cdot PbO_2]$ were synthesized in composition range $5 \leq x \leq 50$mol % Fe_2O_3. XRD analysis reveals that increasing the Fe_2O_3 content above 30 mol% determines the development of the α-Fe_2O_3 crystalline phase in the host matrix.

BIBLIOGRAPHY

1. J. Wong and CA Angell, Spectroscopy in glassy solids (I,II)
2. FF Bentley and Razek, Infrared Spectra and characteristic frequencies 700-300cm $^{-1}$, 1968
3. DHWhiffen, Spectroscopy, London, 1966
4. I. Bratu, P.Oana and M.Culea, study UBB, Phys, 1976
5. Jamnicky M., Znasic P., Tunega D., Ingram MD, 1995, *J. Non-Cryst. Solids* , vol. 185, p. 151
6. Jeyadevan B., Tohji K., Makatsuka K., Narayanasamy A., 2000, *J. Magn. Magn. Mater*,vol. 217, pg. 99
7. Lovchinov V., Nedkov I., 1998, *Nato. Sci. Serum. 3: High Tech* ., vol. 72, pg. 257
8. Tretyakov Yu. D., 2003, *Usp. Chem* ., vol. 72, pg. 731
9. Shihue G., Zontago Z., Mingzhong W., 2003, *Mat. Res. Shock. Symp. Proc* ., vol. 755,pg. 141
10. Strong SL, Kaplow Q., 1968, *Acta Cryst. B.* , vol. 24, p. 1032
11. Eitel W., 1965, *Silicate Science* , Academic Press, New York, vol. 2
12. Ardelean I., Lucacel RC, 2006, *Oxide materials with glassy and ceramic structure. Possibilities of obtaining, some properties and applications* , Cluj University Press, ISBN (10) 973-610-500-8
13. Rada Simona, Culea E., Păscuță P., Rada M., 2013, *Spectroscopic methods of analysis,* UT Press Publishing House, Cluj-Napoca
14. Rada Simona, Culea E., Culea Monica, 2010, *Borate-Tellurate Glasses: An Alternative of Immobilization of the Hazardous Wastes,* Nova Science Publishers, Inc., New York.
15. Rada Simona, Culea E, Culea Monica, 2010, *Borate-Tellurate Glasses: An Alternative of Immobilization of the Hazardous Wastes* , Nova Science Publishers INC., New York, pg.1-89
16. Ardelean I., Lucacel RC, 2006, *Oxide materials with glassy and ceramic structure. Possibilities of obtaining, some properties and applications* , Cluj University Press, ISBN (10) 973-610-500-8
17. Culea Monica, Culea E., 2004, *Physical methods of analysis* , Risoprint Publishing House, Cluj-Napoca, pg.51-79

18. Astilean V., 2002, *Modern methods and techniques of optical spectroscopy* , Ed. Casa Cărții de Știința.
19. Rada Simona, Culea E., Păscuță P., Rada M., 2013, *Spectroscopic methods of analysis,* UT Press Publishing House, Cluj-Napoca
20. Rada Simona, Culea E., Culea Monica, 2010, *Borate-Tellurate Glasses: An Alternative of Immobilization of the Hazardous Wastes,* Nova Science Publishers, Inc., New York.
21. Culea E., 2011, *Course on Environmental Quality Assessment and Analysis Tools*
22. Rada M., Chelcea R., Rada Simona, Rus Loredana, Dura V, Ristoiu T., Rusu T.,Culea E., 2013, *Effect of aluminum oxide codoping on cooper-doped lead-germanate glasses* Spectrochimica Acta A, vol. 102, pg.414-418
23. Rada M., Rus Loredana, Zagrai Mioara, Rada Simona, Culea Monica, Neumann M., Culea E., 2011 , *FTIR, UV-VIS and EPR spectroscopy investigations on the structure of tungsten-lead-borate glasses,* Advanced Spectroscopies on Biomedical and Nanostructured *Systems* , Cluj-Napoca, Romania, September 4-7, PN40
24. Rada Simona, Culea E., Rada M., 2011, Mater. Chem. Phys., vol. 128, pg. 464
25. Rada Simona, Culea Monica, Neumann M., Culea E., 2008, Chem. Phys. Letters, vol. 460, pg. 196
26. Rada M., Maties V., Rada Simona , Culea E., 2010, *J. Non-Cryst. Solids* , vol. 356, pg. 1267-1271
27. P.Geerlings, F.De Proft and W.Langenaeker, Conceptual Density FunctionalTheory, Chem.Rev.2003,103,1793−1873
28. Christopher J. Cramer, Essentials of Computational Chemistry, Theories and Models, 2002
29. David C. Young, Computational Chemistry, A practical Guide for Applying Techniques to Real-World Problems, 2001
30. James B. Foresman, Eleen Frisch, Exploring Chemistry with Electronic Structures Methods, 2001
31. Wolfram Koch, Max C. Holthausen, A Chemist's Guide to Density Functional Theory, 2000
32. Robert G. Parr and Weitao Young, Density – functional theory of atoms and molecules, 1989
33. **S. Mitrici** , S. Rada, E. Culea, L. Pop, A. Popa, A. Bot, Journal of Non Crystalline Solids, 2017 Volume 471 , 1 September 2017, Pages 349-356

34. YB Saddeek, KA Gh. Abbady, N. Afify, KHS Shaaban, A. Dahshan, , Optical and structural evaluation of alumina-bismuth borate glasses doped with different amounts of (Y_2O_3) , J. Non-Cryst. Solids 454 (2016) 13-18.
35. K. Annapoorani, Ch. Basavapoornima, N. S. Murthy, K. Marimuthu, Investigations on the structural and luminescent behavior of Er3+-doped lithium zinc borate glasses for laser and optical amplifier applications , J. Non-Cryst. Solids 447 (2016) 273-282.
36. FH ElBatal, MA Ouis, HA ElBatal, Comparative studies on the bioactivity of some borate glasses and glass-ceramics from the two systems: Na_2O- CaO - B_2O_3 and NaF - CaF_2 - B_2O_3 , Ceram. Int. 42 (2016) 8247-8251.
37. II Kindrat, BV Padlyak, S. Mahlik, B. Kuklinski, YO Kulyk, Spectroscopic properties of the Ce-doped borate glasses , Opt. Mater. 59 (2016) 20-27.
38. Ch. Basavapoornima, K. Linganna, CR Kesavulu, S. Ju, BH Kim, WT Han, CK Jayasankar, Spectroscopic and pump power-dependent upconversion studies of Er^{3+} doped lead phosphate glasses for photonic applications , J. Alloys Compd. 699 (2017) 959-968.
39. G. Lakshminarayana, S. Buddhudu, Spectral analysis of Mn^{2+} , Co^{2+} and Ni^{2+} : B_2O_3 – ZnO–PbO glasses , Spectrochim. Acta A 63 (2006) 295-304.
40. FHA ElBatal, MMI Khalil, N. Nada, SA Desouky, Interaction of Gamma rays with mixed CoO+NiO containing ternary silicate glasses , Mater. Chim. Fiz. 82 (2003) 375-387.
41. H. Wen, P. A. Tanner, B. M. Cheng, Optical properties of lead borate glasses doped with 3d transition metal ions , Mater. Res. Taurus. 83 (2016) 400-407.
42. A. Paul, AN Tiwari, Optical absorption of nickel (II) in Na_2O - NaCl- B_2O_3 and Na_2O - NaBr- B_2O_3 glasses , J . Mater. Science 9 (1974) 1057-1063.
43. FA Khalifa, ZA El-Hadi, FM Ezz El-Din, FA Moustaffa, Infrared absorption spectra of some nickel-containing alkali borate glasses , J. Mater. Sci. Lett. 10 (1991) 1132-1135.
44. L. Liu, X. D. Li, J. Liu, S. Jiang, Y. C. Li, G. Y. Shen, H. K. Mao, Y. Bi, J. Xu, High-pressure structural and elastic properties of NiO up to 67 GPa, J. Appl. Phys. 104 (2008) 113521-1-5.
45. RE Newnham, RP Santoro, P.F. Seal and G.R. Stallings, Antiferromagnetism in Mn3B2O6 , Co3B2O6 and Ni3B2O6, Phys. . Status Solidi B 16 (1966) 17-19.
46. Menaka, SE Lofland, KV Ramanujahary, AK Ganguli, A novel low-temperature methodology to obtain pure nanocrystalline nickel borate , J. Organome. Chem. 695 (2010) 1002-1005.

47. P. Liang, L. Du, X. Wang, ZH Liu, Preparation of $Ni_3B_2O_6$ Nanosheet-based flower-shaped architecture by a precursor method and its electrochemical properties in lithium-ion battery, Solid State Sciences 37 (2014) 131-135.
48. S. Rada , M. Culea, M. Neumann, E. Culea, Structural role of europium ions in lead – borate glasses inferred from spectroscopic and DFT studies , Chem. Phys. Lett. 460 (2008) 196-199.
49. S. Rada, P. Pascuta, M. Culea, V. Maties, M. Rada, M. Barlea, E. Culea, The local structure of europium - lead-borate glass ceramics , J. Molec. Struct. 924-926 (2009) 89-92.
50. S. Rada, T. Ristoiu, M. Rada, I. Coroiu, V. Maties, E. Culea, Towards modeling gadolinium-lead-borate glasses , Mat. Res. Taur. 45 (2010) 69-73.
51. S. Rada, M. Rada, E. Culea, Improved photocatalytic activity of TiO_2 codoped with C, F loaded with AgCI , J. Alloys Compd. 552 (2013) 10-14.
52. S. Rada, P. Pascuta, L. Rus, M. Rada, E. Culea, Spectroscopic properties and ab initio calculations on the structure of erbium–zinc-borate glasses and glass ceramics , J. Non-Cryst. Solids 358 (2012) 30-35.
53. M. Rada , S. Rada , E. Culea, Structural properties of tungsten - lead - borate glasses before and after laser irradiation , J. Non-Cryst. Solids 357 (2011) 2024-2028.
54. S. Rada, M. Zagrai, M. Rada, E. Culea, L. Bolundut, ML Unguresan, M. Pica, Spectroscopic and electrochemical investigations of lead-lead dioxide glasses and vitroceramics with applications for rechargeable lead-acid batteries , Ceram. International 42(3) (2016) 3921-3925.
55. S. Rada, R. Chelcea, M. Rada, A. Bot, N. Aldea, V. Rednic, E. Culea, Electrochemical characterization and structure of tungsten-lead-germanate glasses and glass ceramics , Electrochim.Acta 109 (2013) 82-88.
56. Menaka, S. Sharma, KV Ramanujahary, SE Lofland, AK Ganguli, Size and morphology control of anisotropic nickel borate nanostructures using microemulsions and their magnetic properties , J. Colloid Interface Sci . 360(2) (2011) 393-397.
57. UV - Visible and infrared absorption spectra of transition metal doped lead phosphate glasses and the effect of gamma irradiation J. Non-Cryst. Solids, 355 (2009) 2439-2447.
58. X. Liu, W. Zhu, X. Cui, T. Liu, Q. Zhang, Facile thermal conversion route synthesis, characterization and optical properties of rod-like micron nickel borate , Powder Technol. 222 (2012) 160-165.

59. LDBogomolova, N.A.Krasilnikova, V.V.Tarasova, Electron paramagnetic resonance of nickel-implanted silica glasses , J.Non-Cryst.Solids 319 (2003) 225-231.
60. R. Bottcher, HT Langhammer, T. Muller, Study of the paramagnetic resonance of nickel ions in hexagonal barium titanate , J. Phys. Condens. Materia 23 (2011) 115903-11912.
61. HGHecht, Study of the Structure of Nickel in Soda-Boric Oxide Glasses, J. Chem. Phys. 47 (1967) 1840-1843.
62. B.Sreedhar, CH Sumalatha, K. Kojima, ESR and optical absorption spectra of Ni(II) ions in lithium fluoroborate glasses , J. Mat. Sci. 31, 6 (1996) 1445-1448.
63. RVSSN Ravikumar, J.Yamauchi, AVChandrasekhar, YP Reddy, PS Rao, Identification of chromium and nickel sites in zinc phosphate glasses , J. Mol. Struc. 740 (2005) 169-173.
64. RVSSN Ravikumar , AV . Chandrasekhar , L. Ramamoorthy , BJ . Reddy , YP . Reddy , J. Yamauchi , PS . Rao , Spectroscopic studies of transition metal doped sodium phosphate glasses , J . Alloys Comp d. 364(1-2) (2004)176-179.
65. I. Ardelean, Gh. Ilonca, D. Bărbos, H. Adams, Magnetic properties of *x* NiO. (1- *x*)[2B $_2$ O $_3$ PbO] glasses , Solid State Commun . 40 (1981) 769-770.
66. I. Ardelean, Gh. Ilonca, V. Simon, T. Jurcut, S. Filip, T. Hagau, Magnetic properties of nickel-strontium-borate oxide glasses , J. Mater. Sci. Lett. 16 (1997) 200-201.
67. A. Yadav, S. Khasa, A. Hooda, M. S. Dahiya, A. Agarwal, P. Chand, EPR and impedance spectroscopic investigations on lithium bismuth borate glasses containing nickel and vanadium ions , Spectrochim. Acta A 157 (2016) 129-137.
68. V Singh, MS Seehra, Temperature and size dependence of electron magnetic resonance spectra of Ni nanoparticles embedded in an $_{\text{amorphous}}$ SiO 2 matrix , J. Phys.: Condens. Matter 21 (2009) 456001-4560009
69. JM Gonzalez-Calbet, M. Vallet-Regi, MJ Sayagues RD Sanchez, MT Causa, EPR and magnetization of La $_2$ NiO $_4$, J. Mater. Res. 9(1) (1994) 176-179.
70. F. Albert Cotton, G. Wilkinson, Advanced Inorganic Chemistry, Wiley Eastern Ltd., New Delhi, 1976 (pp. 894-896).
71. GS Rao, BK Sudhakar, HNL Prasanna, V. Devasahayam, MVSCS Rao, Spectroscopic studies of nickel oxide doped lead arsenate glasses , J. Non-Cryst. Solids 357 (2011) 1130-1135.

72. B. Johnson, NRK Chand, BK Sundhakar, GS Rao, Chemical durability, thermal stability and spectroscopic studies of the influence of Ni^{2+} ions in oxyfluorophosphate glasses , J. Mater. Sci.: Mater. Electron. 27 (2016) 8833-8847.
73. SVGVA Prasad, MS Reddy, N. Veeraiah, Nickel ions - A structural probe in $BaO-Al_2O_3-P_2O_5$ glass system through dielectric, spectroscopic and magnetic studies ,J. Fiz. Chim. Solids 67 (2006) 2478-2488.
74. MR Kalaie, AA Youzbashi, MA Meshkot, FH Nasab, Preparation and characterization of superparamagnetic nickel oxide particles by chemical route, Appl. Nanosci. 6 (2016) 789-795.
75. S. Sako, Y. Umemura, K. Ohshima, M. Sakai, Magnetic property of ultrafine antiferromagnetic MnO particles , J. Phys. Soc. Jpn. 65 (1995) 280-284.
76. GN Rao, YD Yao, JW Chen, Superparamagnetic behavior of antiferromagnetic CuO nanoparticles, IEEE Transactions on Magnetics 41(10) (2005) 3409-3411.
77. F. Bodker, MF Hansen, C. Bender Koch, K. Lefmann, S. Morup, Magnetic properties of hematite nanoparticles **,** Phys. rev. B61 (2000) 6826-6838.
78. Oh . Pana, C. Leostean, ML Soran, M. Stefan, S. Macavei, S. Gutoiu, V. Pop, O. Chauvet, Synthesis and characterization of Fe–Pt based multishell magnetic nanoparticles , J. Alloys Compd. 574 (2013) 477-485.
79. P. Pascuta, A. Vladescu, Gh. Borodi, E. Culea, R. Tetean, Structural and magnetic properties of zinc ferrite embedded in amorphous matrix , Ceram. Int. 37 (2011) 3343-3349.
80. **S.Mitrici,** S.Rada, E. Culea, LDavid, A.Bot, Journal of Non-Crystalline Solids, Volume 458, 15 February 2017, Pages 34-40
81. S. Chaudharia, M. Srinivasan, J. Mater. Chem 22 (2012) 23049.
82. RS Devan, RA Patil, JH Lin, YR Ma, Adv. Mater Func. 22(16) (2012) 3326.
83. A. Figuerola, RD Corato, L. Manna, T. Pellegrino, Pharmacological Research 62 (2010) 126.
84. K. Woo, HJ Lee, JP Ahn, YS Park, Advanced Materials 15(20) (2003) 1761.
85. R. Zboril, M. Mashlan, D. Petridis, Chem. Mater. 14(3) (2002) 969.
86. DM Yufanyi, AM Ondoh, J. Foba-Tendo, KJ Mbadcam, Amer. J. Chem. 5(1) (2015) 1.
87. G. Xinglong, W. Guoxiu, P. Jinsoo, L. Hao, Y. Juan, Nanotechnology 19(12) (2008) 125606.

88. S. Bharathi, D. Nataraj, D. Mangalaraj, Y. Masuda, K. Senthil, K. Yong, K., J. Physics D: Applied Physics 43(1) (2010) 015501.
89. M. Hermanek, R. Zboril, I. Medrik, J. Pechousek, C. Gregor, J. Amer. Chyme. Shock. 129 (2007) 10929.
90. G. Tong, J. Guan, Z. Xiao, X. Huang, Y. Guan, J. Nanoparticle Research, 12 (2010) 3025.
91. H. Li-Chieh, L. Yuan-Yao, L. Chih-Geng, H. Chieh-Wei, C. Gung, J. Physics D: Applied Physics 41(18) (2008) 185003.
92. S. Chakrabarty, TK Jana, K. De, S. Das, K. Dey, K. Chatterjee, Mater. Research Express 1(4) (2014) 046104.
93. RE Bird, RL Hulstrom, L. Lewis, J. Sol. Energy 30 (1983) 563.
94. S. Rada , T. Ristoiu, M. Rada, I. Coroiu, V. Maties, E. Culea, Mater. Res. Taur. 45 (2010) 69.
95. M. Rada , S. Rada , E. Culea , J. Non-Cryst. Solids 357 (2011) 2024.
96. S. Rada, L. Rus, M. Rada, M. Zagrai, E. Culea, T. Rusu, Ceram. International 40 (2014) 15711.
97. S. Rada , A. Dehelean , E. Culea , J. Molecular Modeling , 17(8) (2011) 2103.
98. R. Chelcea, S. Rada , E. Culea, M. Rada, Spectrochim. Acta Part A 79(3) (2011) 481.
99. S. Rada , M. Culea, M. Neumann, E. Culea, Chem. Phys. Letters 460 (2008) 196.
100. S. Rada , P. Pascuta, M. Bosca, M. Culea, L. Pop, E. Culea, Vibrat. Spectrosc. 48(2) (2008) 255.
101. S. Rada, R. Chelcea, M. Rada, A. Bot, N. Aldea, V. Rednic, E. Culea, Electrochimica Acta 109 (2013) 82.
102. L. Rus, S. Rada, V. Rednic, E. Culea, M. Rada, A. Bot, N. Aldea, T. Rusu, J. Non-Cryst. Solids 402 (2014) 111.
103. R. Stefan, P. Pascuta, A. Popa, O. Raita, E. Indrea, E. Culea, J. Phys. Chim. Solids 73 (2012) 221.
104. S. Yin, ER Bernstein, Intern. J. Mass Spectroscopy 321-322 (2012) 49.
105. LF Liao, CF Lien, JL Lin, Phys. Chyme. Chyme. Phys. 3 (2001) 3831.
106. AV Golovkin, DI Davlyatshin, AL Serebrennikova, LV Serebrennikov, J. Molec. Struct. 1049 (2013) 392.
107. HG Cho, L. Andrews, J. Molec. Spectrocopy 310 (2015) 84.

108. Ratna Saria ,, Zahira Yaako, Manal Ismail, Wan Ramli Wan Daud, Lukman Hakim- Ceramics International, Vol. 39, 2013, 3211-3219

109. Zichun Wanga, Suman Pokhrel, Mengmeng Chena, Michael Hungerc, Lutz Mädler, Jun Huanga- Journal of Catalysis, Vol. 302, 2013, 10-19

110. Andrzej Gnieweka, Józef J. Ziółkowskia, Anna M. Trzeciaka, Mirosław Zawadzkib, Hanna Grabowskab, Józef Wrzyszczb- Journal of Catalysis 254 (2008) 121–130

111. Nina Kostevˇ seka, Kristinaˇ Zuˇ zek Roˇ zmana, Darja Peˇ ckoa, Boris Pihlarb, Spomenka Kobe- Electrochimica Acta 125 (2014) 320–329

112. Sundeep Mukherjeea, Marcelo Carmob, Golden Kumara, Ryan C. Sekolb, André D. Taylorb, Jan Schroersa, - Electrochimica Acta, 74, 2012, 145-150

113. Yu.P. Mitrofanov, M. Peterlechner, I. Binkowski, M.Yu. Zadorozhnyy, IS Golovin, c SV Divinskia and G. Wildea- Acta Materialia , 90, 2015, 318-329

114. Ying Liua,b, Sheng Wanga, Tianjun Suna, Diannan Gaoa, Chunxi Zhanga, Shudong Wanga,- Applied Catalysis B: Environmental,119–120, 2012, 321-328

115. S. Sako, Y. Umemura, K. Ohshima, M. Sakai, Magnetic property of ultrafine antiferromagnetic MnO particles , J. Phys. Soc. Jpn. 65 (1995) 280-284.

116. A. Fahmi and RA van Santen, J. Phys. Chem., 1996, 100,5676-5680

117. Nakatsuji, H.Hada, M.Yonezawa, TJAm.Chem. Shock. 1987,109,1902

118. Blomberg, MRA, Siegbahn, PE, M, Svensson, MJPhys. Chem., 1992, 96, 5783

119. Fayet, T. Kaldor, A. Cox, DMJ Chem. Phys. , 1990 , 92, 254

120. Parks, EKZhu, L. Riley, J. Chem. Phys., 1994, 100, 7206

121. J. Wong and CA Angell, Spectroscopy in glassy solids (I,II)

122. FF Bentley and Razek, Infrared Spectra and characteristic frequencies 700-300cm $^{-1}$, 1968

123. DHWhiffen, Spectroscopy, London, 1966

124. I. Bratu, P.oana and M.Culea, study UBB, Phys, 1976

125. Strong SL, Kaplow Q., 1968, *Acta Cryst. B.* , vol. 24, p. 1032

126. Eitel W., 1965, *Silicate Science* , Academic Press, New York, vol. 2

127. Ardelean I., Lucacel RC, 2006, *Oxide materials with glassy and ceramic structure. Possibilities of obtaining, some properties and applications* , Cluj University Press, ISBN (10) 973-610-500-8

Published articles

1. Nickel-lead-borate glasses and vitoceramics with antiferromagnetic NiO and nickel-orthoborate crystalline phases

S. Mitrici, S.Rada, E.Culea, L.Pop, A.Popa, A.Bot, Journal of Non-Crystalline Solids, Volume 471 , 1 September 2017, Pages 349-356; IF = 2.5; AIS = 0.4;

2. Acetylene adsorption on the iron-lead-borate glassy and vitroceramic surface

S. Mitrici, S.Rada, E.Culea, L.David, A.Bot, Journal of Non-Crystalline Solids, Volume 458, 15 February 2017, Pages 34-40; IF = 2.5; AIS = 0.4;

Conference participation:

TIM 24 Physics Conference – Adsorption of acetylene on lead-based glass-ceramics surfaces doped with nickel and palladium (oral presentation) West University of Timișoara - Faculty of Physics, Timișoara, Romania between 30th of May 2024 – 1st of June 2024